Supporting Information

Scaffolding Protein Mimics Using a DNA Nanostructure

Fangzhou Zhao[a], Tianxiao Yang[b], Daniel Saliba[a], Ziyi Sun[a], Trishalina Das[a], Jathavan Asohan[a], Yihao Wu[a], Alba Guarné[b], and Hanadi F. Sleiman[a]*

[a]Department of Chemistry and Centre de Recherche en Biologie Structurale, McGill University, 801 Sherbrooke St. W., Montreal, QC, Canada

[b]Department of Biochemistry and Centre de Recherche en Biologie Structurale, McGill University, 3649 Promenade Sir William Osler, Montreal, QC, Canada

*E-mail: hanadi.sleiman@mcgill.ca

Table of Contents

I. Materials

SigmaAldrich supplied ferrous sulfate ($FeSO_4$) and zinc sulfate ($ZnSO_4$). ChemGenes supplied 1 μmol Universal 1000Å LCAA-CPG solid supports and automated DNA synthesis reagents. Glen supplied 5'-DBCO-TEG phosphoramidite for the modification of single-stranded DNA (ssDNA) on solid support. MedChemExpress supplied ferroheme. TCI supplied 3,5-di-tert-butyl-1,2-benzoquinone. Oakwood chemical supplied 3,5-di-tert-butylcatechol. BioShop supplied EDTA, agarose and tris. VWR provided GelRed™. Thermofisher supplied glacial acetic acid, GeneRuler Ultra Low Range DNA ladder, and GeneRuler DNA Ladder Mix. AK Scientific supplied 5-azidopentanoic acid for the modification of peptide strand on resin. CEM Corporation supplied automated solid phase peptide synthesis reagents.

1xTAMg buffer contains 45 mM Tris and 12.5 mM $MgCl_2$•$6H_2O$ with a pH of 8.0 adjusted with glacial acetic acid. The composition of the 1xTAE buffer is 40 mM Tris, 20mM acetate and 1mM EDTA with a pH of 8.3. 1xNaF buffer (pH = 7.4) contains 138.2 mM NaF, 10mM Na_2HPO_4 and 1.8 mM NaH_2PO_4. 1xMES buffer contains 100 mM MES and 130 mM NaCl with a pH of 6.5, which was deoxygenated by repeating the freeze-thaw cycles three times. The mobile phase of TEAA is 50 mM triethylammonium acetate with a pH of 7.0 that has been adjusted with glacial acetic acid.

II. Instrumentation

The oligonucleotide sequences were generated using standard automated solid-phase oligonucleotide synthesis on a 1 μmol scale using a BioAutomation MerMade MM6 DNA synthesizer. The peptide strands were produced using standard automated solid phase peptide synthesis on a 0.01 mmol scale using a CEM Liberty Blue 2.0 peptide synthesizer. Using Bio-Rad

Laboratories' ChemiDoc™ MP System, gel images were collected. Using a NanoDrop One Spectrophotometer, quantitative measurements of ultraviolet-visible (UV-vis) absorbance at 260 nanometers (OD260) were performed. The molar extinction coefficient at 260 nm provided by IDT was used for the concentration calculations. Single stranded DNA-peptide conjugates were purified by Agilent 1260 Infinity HPLC (high performance liquid chromatography) system equipped with a Hamilton PRP-1 RP (reverse phase) column. Using an Applied Biosystems ProFlex PCR system, DNA nanostructures were subjected to thermal annealing. Circular Dichroism (CD) was performed on JASCO J-810 spectropolarimeter equipped with a xenon lamp in a 1 mm path length quartz cuvette. UV-vis spectroscopy was performed in a Cary UV-vis Multicell Peltier. Iron oxidation kinetic scans were performed in a Horiba spectrometer with a TgK Scientific SFA-20 apparatus. Kinetic absorbance data was acquired in a BioTek Cytation 5 plate reader. Using a Dionex Ultimate 3000 linked to a Bruker MaXis Impact™ QTOF, LC-ESI-MS was performed. AFM imaging was performed under ambient air conditions using a MultiMode8™ SPM connected to a Nanoscope™ controller from Veeco. Images were acquired using tapping mode with a ScanAsyst-Air triangular silicon nitride probe (k = 0.4 N/m, tip radius = 2 nm, and f_o = 70 kHz; from Bruker).

III. Structure modeling

The model of DNA cube scaffold was generated and optimized in OxDNA.[1] Each edge of the cube was found to be around 10 nm (**Figure S1A**). The polypeptide model was predicted by AlphaFold (**Figure S1B**). To ensure sufficient distance for peptides to interact with each other within the scaffold, a 6-thymindine spacer was placed between the DBCO-TEG modification and the DNA moiety. Upon click reaction, the DBCO-TEG-6T-DNA can be conjugated to azido-peptide by a covalent linker (**Figure S1C**).

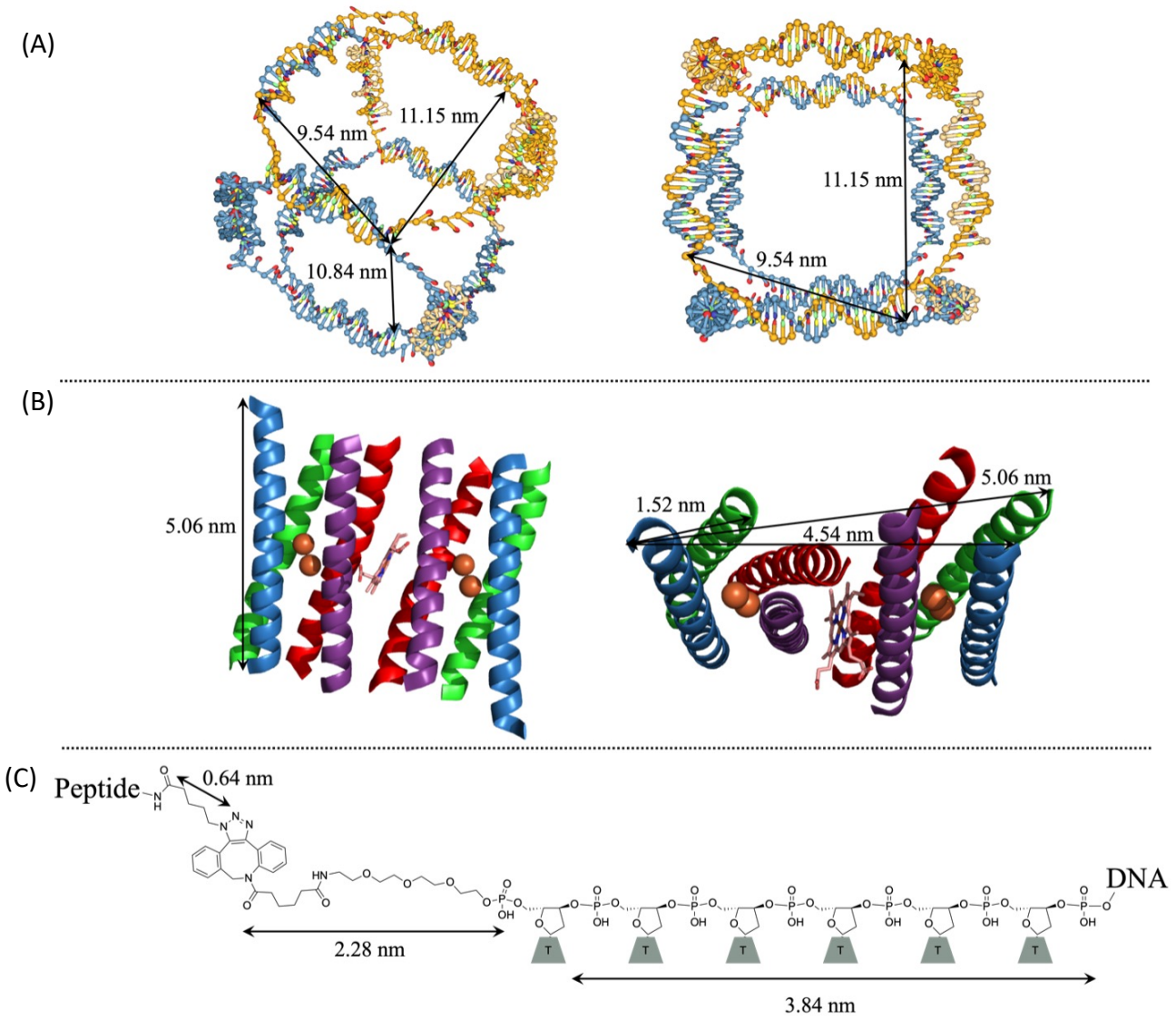

Figure S1. (A) Structure of DNA cube scaffold was predicted by MD simulations in OxDNA. (B) Structure of polypeptide was predicted by AlphaFold. (C) Estimated length of the covalent linkage between peptide and DNA.

To rigidify the DNA scaffold, splint strands were designed to diagonally bridge adjacent edges. Splint lengths and geometries were optimized using OxDNA simulation. As shown in **Figure S2A**, splint strands with excessively long corner regions (4 T) induce cube distortion. In contrast, splint strands with 2 T turning corners adopt a more favorable conformation without disrupting the overall cube geometry (**Figure S2B**). Therefore, the splint 2 T was used to rigidify both rims of

the scaffold. A normal DNA cube (**Figure S2C**) and rigidified DNA cube (**Figure S2D**) were built and simulated in OxDNA. The enhanced rigidity of the splinted structure is reflected by reduced RMSF values obtained from molecular dynamics simulations (**Figure S2E**).

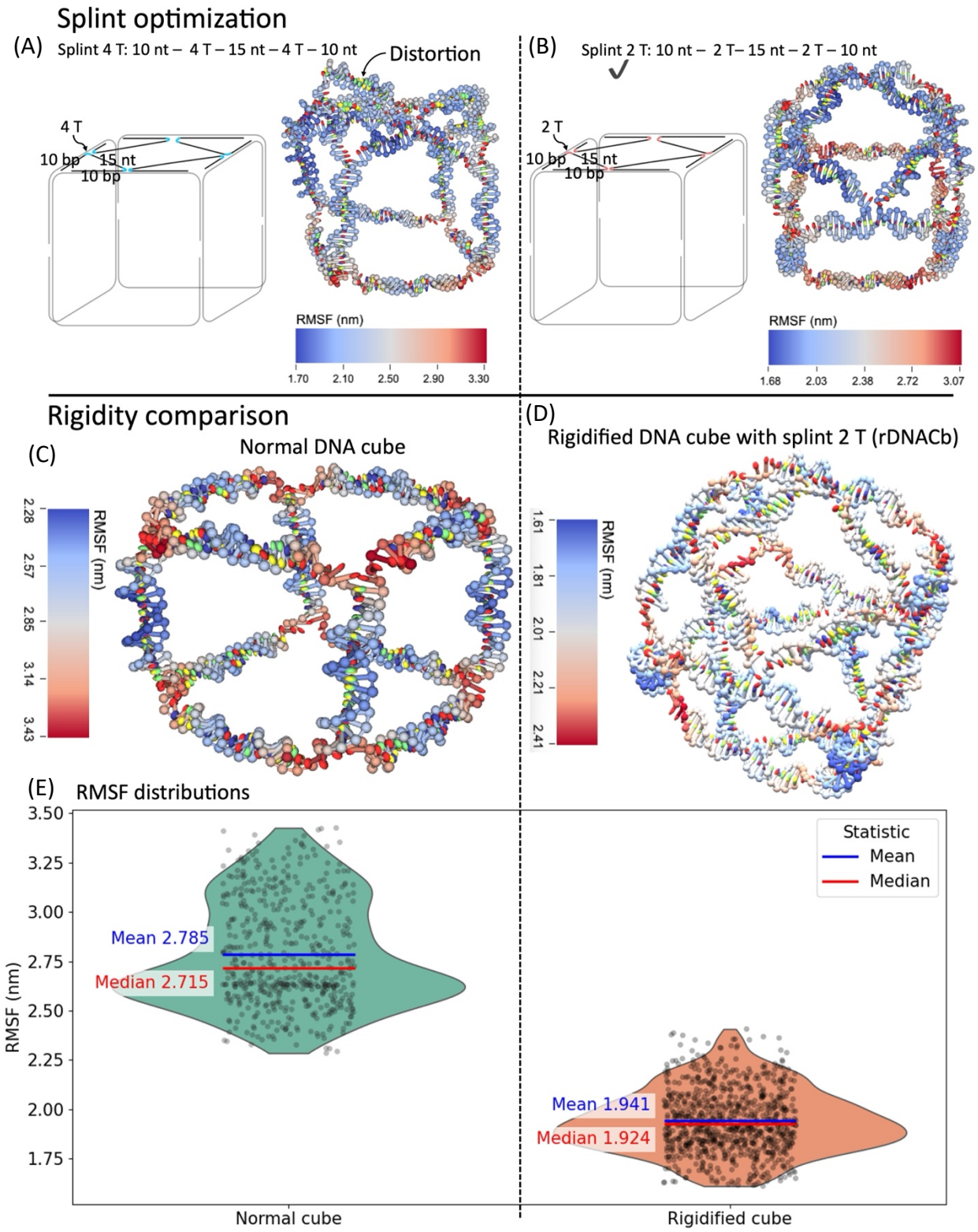

Figure S2. Schematic representations and OxDNA simulation results of DNA cubes with splint 4 T (A) and splint 2 T (B). OxDNA simulation results of normal DNA cube (C) and rigidified DNA cube with splint 2 T on both rims (D). Their RMSF distributions are shown in (E).

IV. DNA sequences

Description	Name	Sequences (5'-3')
Cube scaffold strands	1BA	TCGCTGAGTATTTTTCCTATATGGTCAACTGCTCTTTTGCA AGTGTGGGCACGCACACTTTT TATATGGTCAACTGA GGAGTTTTTCACAAATCTG
	2HC	CTATCGGTAGTTTTTCTTCTATACTGGCAATTTGTTTTTACT CAGCGACAGATTTGTGTTTTCATACTCTGCCGTAAGAGGA TTTTCAACTAGCGG
	3ED	CACTGGTCAGTTTTGATCGCCACTAACCTTATATTTTTCTA CCGATAGCCGCTAGTTGTTTTTGGCCTTGGTCCATAAGCG ATTTTGGTTTGCTGA
	4IF	CCACACTTGCTTTTTACGCAACTGAGGTCGCCTCTTTTCT GACCAGTGTCAGCAAACCTTTTGTAACCGCGACTGCGAG AGTTTTTGTGTGCGTGC
Rigidified cube scaffold strands	L1	TCGCTGAGTATTTTTCTGATTGTGTGATAACTTGTTTTGCA AGTGTGGGCACGCACACTTTTACTGTAGTGAGTATACCAA CTTTTCACAAATCTG
	L2	CTATCGGTAGTTTTATGATCTGACTGAATACTCTTTTT TACTCAGCGACAGATTTGTGTTTTGATACACTCATGTCAA TCTGTTTTCAACTAGCGG
	L3	CACTGGTCAGTTTTAGCATCATCTCTGACTGTCATTTT CTACCGATAGCCGCTAGTTGTTTTGAGCTTAGATGTCATTA GCATTTTGGTTTGCTGA
	L4	CCACACTTGCTTTTGACTCTAGACATTGCATGTCTTTT CTGACCAGTGTCAGCAAACCTTTTGTGACGTATGAACATC GCTCTTTTGTGTGCGTGC
Rigidified cube splint strands	1F2	GTTGGTATACTTGTAACCGCGACTGCGTTTGAGTGTATC
	2A3	CAGATTGACATTTATATGGTCAACTGATTATCTAAGCTC
	3C4	TGCTAATGACTTCATACTCTGCCGTAATTCATACGTCAC
	4D1	GAGCGATGTTTTTGGCCTTGGTCCATATTTCACTACAGT

	2I1	AGAGTATTCATTTACGCAACTGAGGTCTTCACAATCAGA
	1E4	CAAGTTATCATTGATCGCCACTAACCTTTGTCTAGAGTC
	4H3	GACATGCAATTTTCTTCTATACTGGCATTAGATGATGCT
	3B2	TGACAGTCAGTTTCCTATATGGTCAACTTGTCAGATCAT
DBCO strands with 6T spacer	B	/DBCOTEG/TTTTTTGTTGACCATATAGGA
	A	/DBCOTEG/TTTTTTTCAGTTGACCATATA
	H	/DBCOTEG/TTTTTTTGCCAGTATAGAAGA
	C	/DBCOTEG/TTTTTTTTACGGCAGAGTATG
	E	/DBCOTEG/TTTTTTAGGTTAGTGGCGATC
	D	/DBCOTEG/TTTTTTTATGGACCAAGGCCA
	I	/DBCOTEG/TTTTTTGACCTCAGTTGCGTA
	F	/DBCOTEG/TTTTTTCGCAGTCGCGGTTAC
DBCO strands without 6T spacer	sB	/DBCOTEG/GTTGACCATATAGGA
	sA	/DBCOTEG/TCAGTTGACCATATA
	sH	/DBCOTEG/TGCCAGTATAGAAGA
	sC	/DBCOTEG/TTACGGCAGAGTATG
	sE	/DBCOTEG/AGGTTAGTGGCGATC
	sD	/DBCOTEG/TATGGACCAAGGCCA
	sI	/DBCOTEG/GACCTCAGTTGCGTA
	sF	/DBCOTEG/CGCAGTCGCGGTTAC
DBCO strands with 6T spacer and complementary overhangs to SNA	Bn	/DBCOTEG/TTTTTTGTTGACCATATAGGATTTTTTTTAATCTCTTTACTGATATA
	En	/DBCOTEG/TTTTTTAGGTTAGTGGCGATCTTTTTTTTAATCTCTTTACTGATATA
	Hn	/DBCOTEG/TTTTTTTGCCAGTATAGAAGATTTTTTTTAATCTCTTTACTGATATA

	In	/DBCOTEG/TTTTTTGACCTCAGTTGCGTATTTTTTTTAATC TCTTTACTGATATA
SNA component strands	SNA[#]	ZZZZZZZZZZZZTTTT**U***A***U*** **U***C***A***G***U***A*** **E***A***G***A***G***A***U***U***U*** **A***a***u***A***
Displacing strands	Bf	GAGCAGTTGACCATATAGGA
	Af	ACTCCTCAGTTGACCATATA
	Hf	CAAATTGCCAGTATAGAAGA
	Cf	TCCTCTTACGGCAGAGTATG
	Ef	ATATAAGGTTAGTGGCGATC
	Df	TCGCTTATGGACCAAGGCCA
	If	GAGGCGACCTCAGTTGCGTA
	Ff	ACTCTCGCAGTCGCGGTTAC

Table S1. DNA sequences used in this study. [#]: **Bold** letters represent 2'-Methoxy (2'-OMe) modifications, while *italicized* letters denote 2'-fluoro (2'-F) modifications. Uppercase letters correspond to phosphodiester (PO) linkages, and lowercase letters indicate phosphorothioate (PS) linkages. Z refers to a C12 modification.[2]

V. Peptide sequences

Name	Sequences (N terminus-C terminus)
BF1 (analog to *E. coli* Bfr helix A)	/5-Azidopentanoic Acid/TKVINYLNKLLGNELVAINQYFLHARMFKNG/COOH/
BF2 (analog to *E. coli* Bfr helix B)	/5-Azidopentanoic Acid/KRLNDVEYHESIDEMKHADRYIERILFLG/COOH/
BF3 (analog to *E. coli* Bfr helix C)	/5-Azidopentanoic Acid/VEEMLRSDLALELDGAKNLREAIGYADSG/COOH/
BF4 (analog to *E. coli* Bfr helix D)	/5-Azidopentanoic Acid/YVSRDMMIEILRDEEGHIDWLETELDLIQKG/COOH/
BF2M1	/5-Azidopentanoic Acid/KRLNDVEYHESIDLMKNADRYIERILFLG/COOH/

BF4M1	/5-Azidopentanoic Acid/YVSRDMMIEILRDLEGNIDWLETELDLIQKG/COOH/
BF2M2	/5-Azidopentanoic Acid/KRLNDVEYHESIDELKHADRYIERILFLG/COOH/

Table S2. Peptide sequences used in this work. Metal-binding residues were labelled in red. Heme-binding residues were labelled in green. Mutated residues were labelled by underlines.

VI. DNA-peptide conjugates preparation

1. Synthesis and purification of single stranded DNA-peptide conjugates

DBCO-DNA and N_3-peptide were synthesized separately from solid phase. Afterwards, 15 nmol DBCO-DNA is mixed with 40 nmol peptide in 100 μL 1xPBS buffer (pH = 7.4). The reaction mixture is incubated at 37 °C overnight, and then purified by RP-HPLC (**Figure S3**). The product containing fractions are lyophilized. The conjugation yield and HPLC patterns are independent to DNA sequences considering their negligible contribution to the hydrophobicity difference. Instead, they are dominated by the net charge, hydrophobicity, and water solubility of peptide sequences. It's noted that conjugation to positively charged peptide BF1 has a lower yield of ~20%, whereas the yield is ~60-70% for conjugation to the other negatively charged peptides.

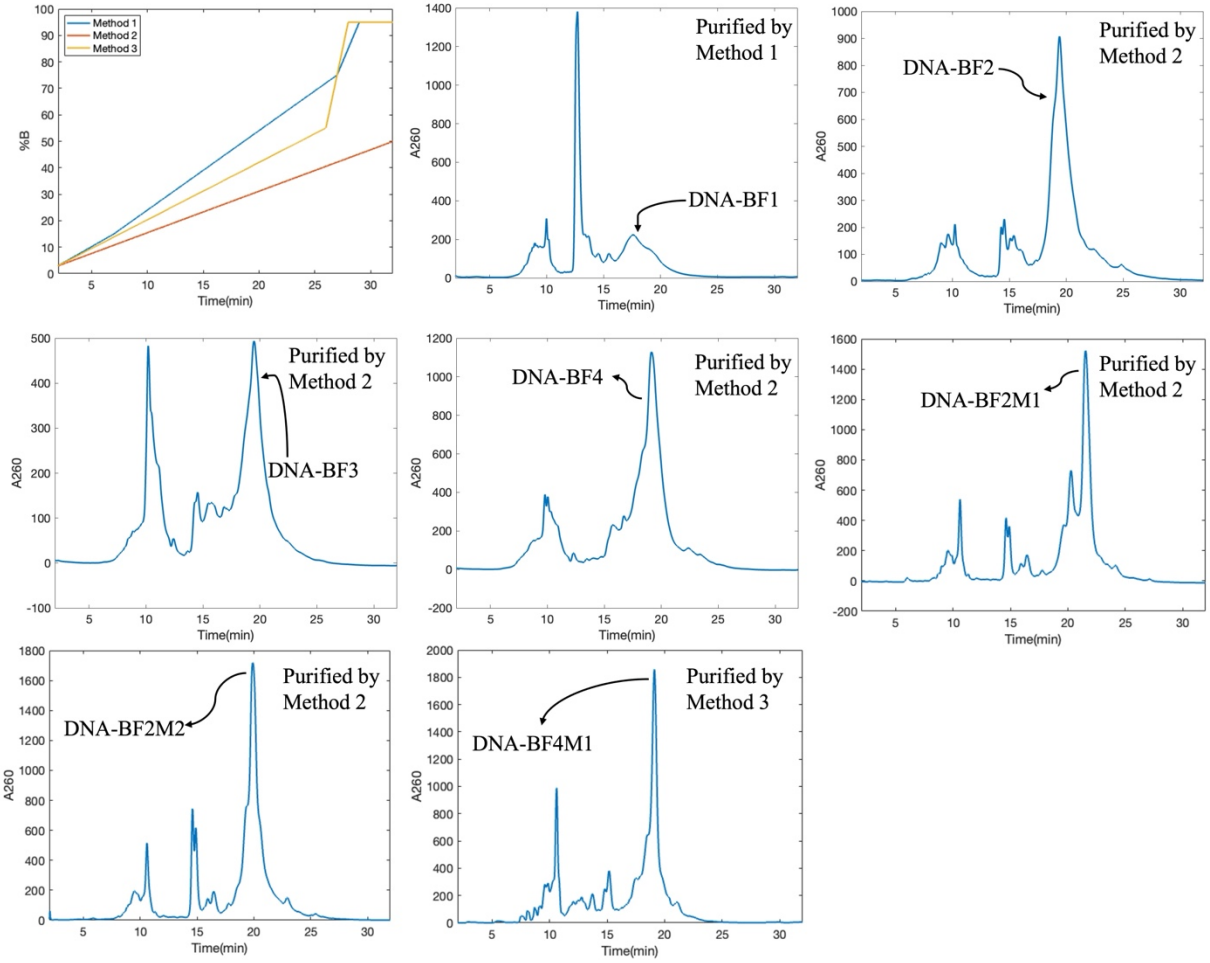

Figure S3. HPLC methods and A260 chromatographs of DNA-peptide conjugates' purification. Solvent A: 50 mM TEAA aqueous buffer, pH = 7.0; solvent B: acetonitrile.

2. MS characterisation of DNA-peptide conjugates

The HPLC-purified DNA-peptide conjugates were submitted to MS analysis. We noticed that DNA-BF1 conjugates can only be detected by MS in buffer with a high salt concentration (1xPBS). This suggests that the salt can eliminate random electrostatic interactions between the two oppositely charged blocks (DNA has negatively charged backbones, whereas BF1 has a positive net charge). Therefore, DNA-BF1 (**Figure S4A**) conjugates were analyzed by MS in 1xPBS buffer. The other conjugates were desalted by Amicon 3K prior to MS analysis.

(A)

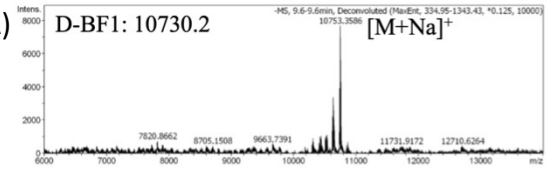
D-BF1: 10730.2
[M+Na]+
10753.3586
7820.8662
8705.1508
9663.7391
11731.9172
12710.6264

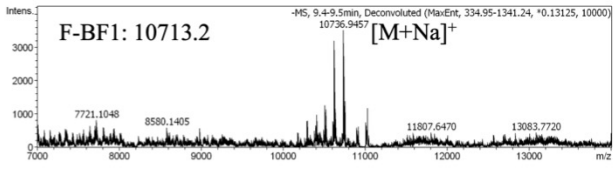
F-BF1: 10713.2
[M+Na]+
10736.9457
7721.1048
8580.1405
11807.6470
13083.7720

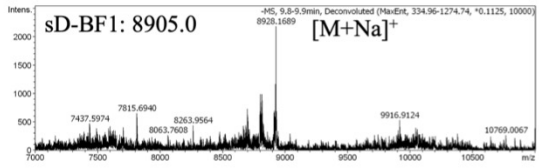
sD-BF1: 8905.0
[M+Na]+
8928.1689
7437.5974
7815.6940
8063.7608
8263.9564
9916.9124
10769.0067

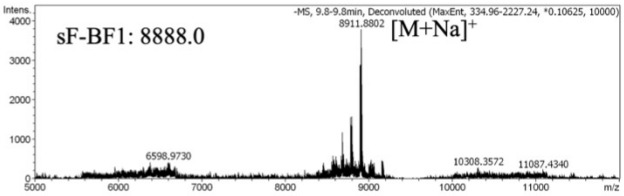
sF-BF1: 8888.0
[M+Na]+
8911.8802
6598.9730
10308.3572
11087.4340

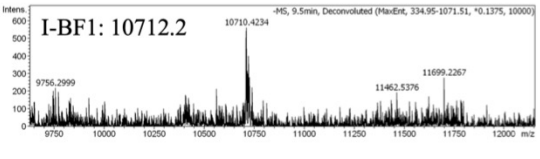
I-BF1: 10712.2
10710.4234
9756.2999
11462.5376
11699.2267

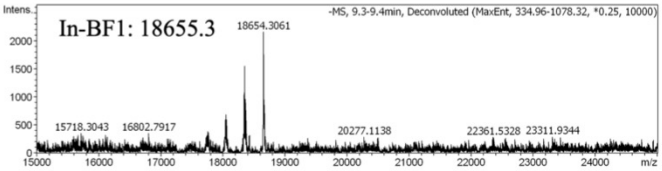
In-BF1: 18655.3
18654.3061
15718.3043
16802.7917
20277.1138
22361.5328
23311.9344

(B)

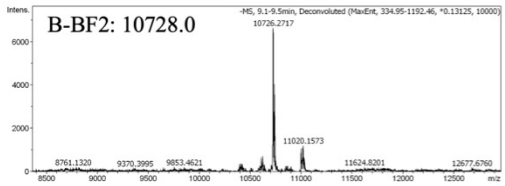
B-BF2: 10728.0
10726.2717
8761.1320
9370.3995
9853.4621
11020.1573
11624.8201
12677.6760

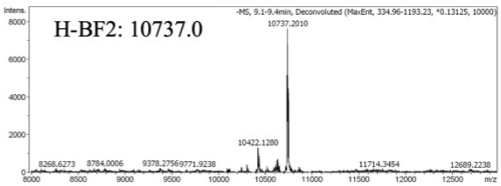
H-BF2: 10737.0
10737.2010
8268.6273
8784.0006
9378.2756
9771.9238
10422.1280
11714.3454
12689.2238

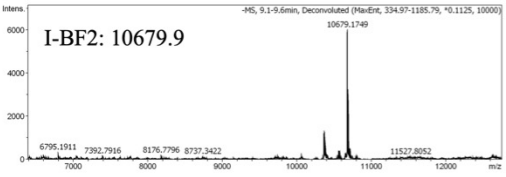
I-BF2: 10679.9
10679.1749
6795.1911
7392.7916
8176.7796
8737.3422
11527.8052

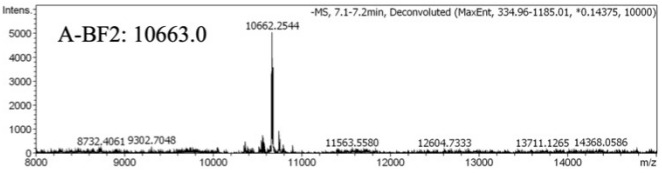
A-BF2: 10663.0
10662.2544
8732.4061
9302.7048
11563.5580
12604.7333
13711.1265
14368.0586

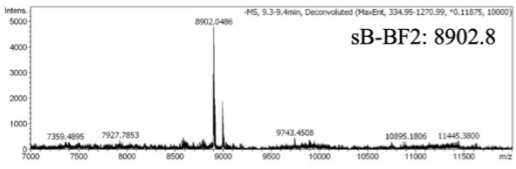
sB-BF2: 8902.8
8902.0486
7359.4895
7927.7853
9743.4508
10895.1806
11445.3800

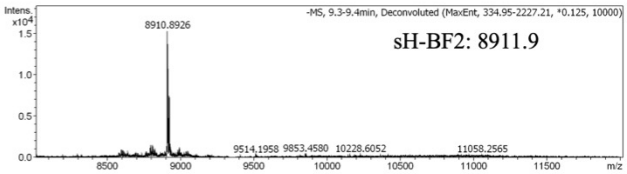
sH-BF2: 8911.9
8910.8926
9514.1958
9853.4580
10228.6052
11058.2565

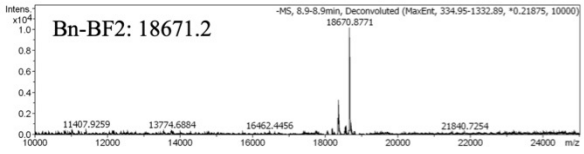
Bn-BF2: 18671.2
18670.8771
11407.9259
13774.6884
16462.4456
21840.7254

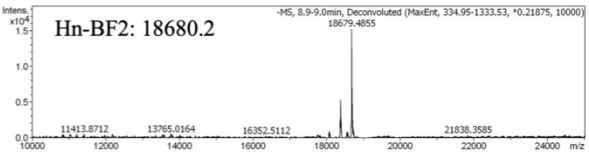
Hn-BF2: 18680.2
18679.4855
11413.8712
13765.0164
16352.5112
21838.3585

(C)

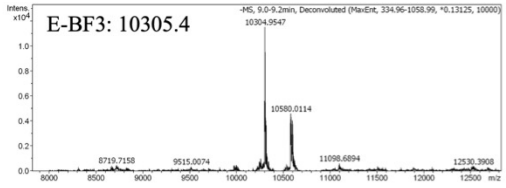
E-BF3: 10305.4
10304.9547
10580.0114
8719.7158
9515.0074
11098.6894
12530.3908

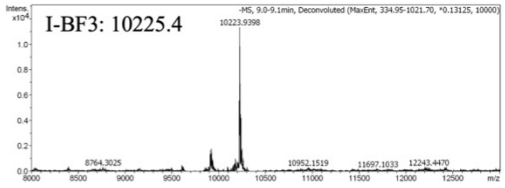
I-BF3: 10225.4
10223.9398
8764.3025
10952.1519
11697.1033
12243.4470

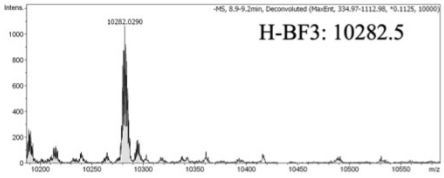
H-BF3: 10282.5
10282.0290

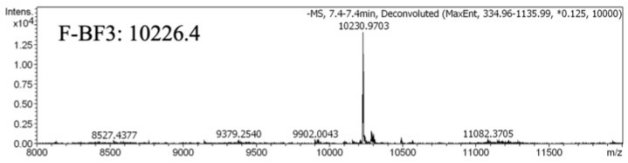
F-BF3: 10226.4
10230.9703
8527.4377
9379.2540
9902.0043
11082.3705

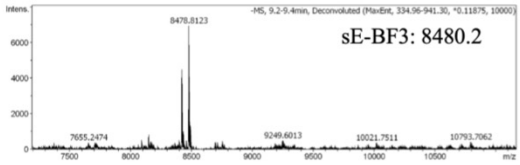
sE-BF3: 8480.2
8478.8123
7655.2474
9249.6013
10021.7511
10793.7062

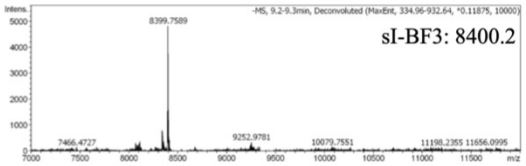
sI-BF3: 8400.2
8399.7589
7466.4727
9252.9781
10079.7551
11198.2355
11656.0995

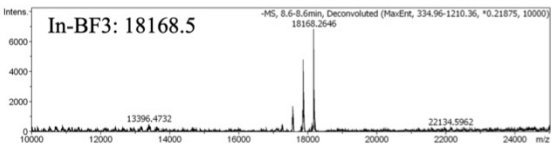
In-BF3: 18168.5
18168.2646
13396.4732
22134.5962

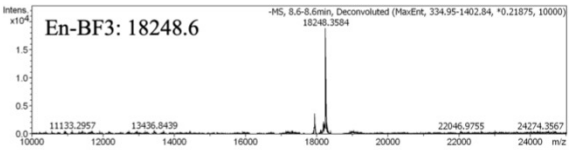
En-BF3: 18248.6
18248.3584
11133.2957
13436.8439
22046.9755
24274.3567

(D)

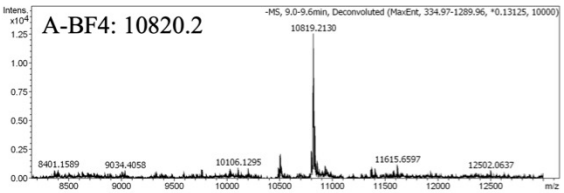
A-BF4: 10820.2
10819.2130
8401.1589
9034.4058
10106.1295
11615.6597
12502.0637

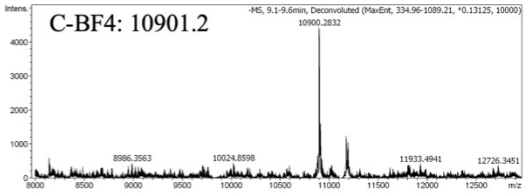
C-BF4: 10901.2
10900.2832
8986.3563
10024.8598
11933.4941
12726.3451

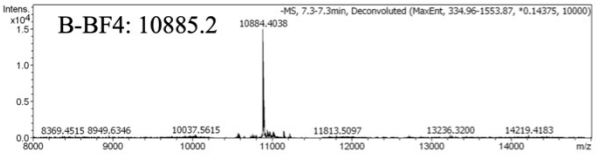
B-BF4: 10885.2
10884.4038
8369.4515
8949.6346
10037.5615
11813.5097
13236.3200
14219.4183

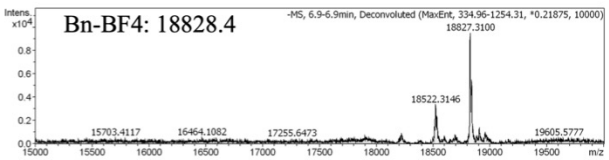
Bn-BF4: 18828.4
18827.3100
18522.3146
15703.4117
16464.1082
17255.6473
19605.5777

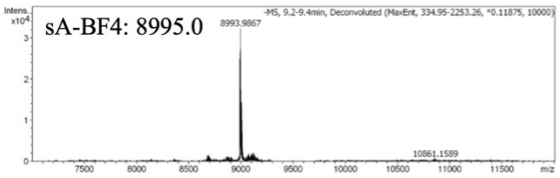
sA-BF4: 8995.0
8993.9867
10861.1589

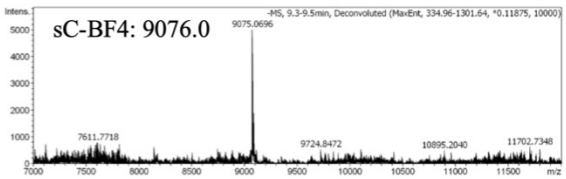
sC-BF4: 9076.0
9075.0696
7611.7718
9724.8472
10895.2040
11702.7348

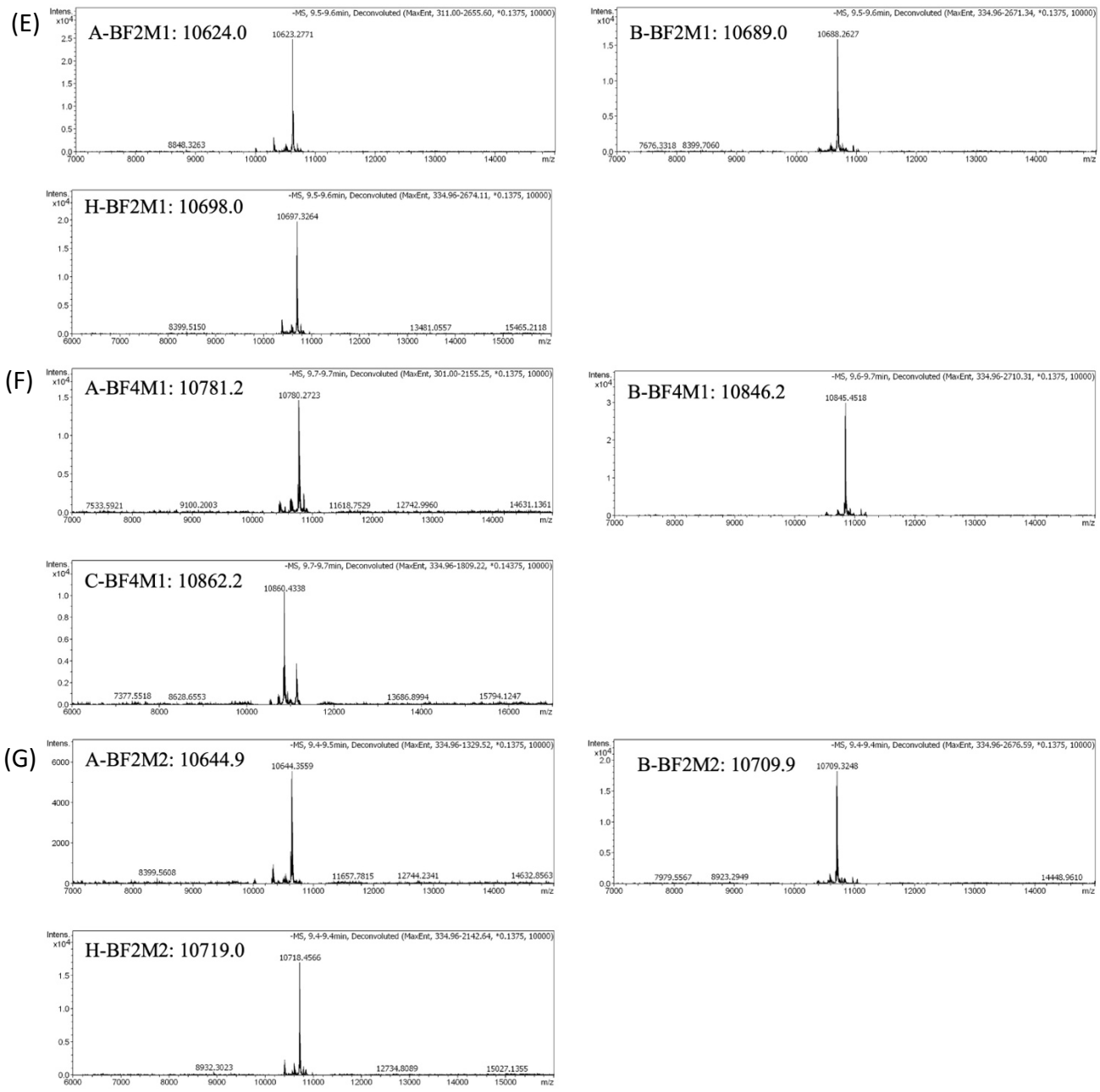

Figure S4. MS data of the DNA-peptide conjugates. (A) DNA-BF1; (B) DNA-BF2; (C) DNA-BF3; (D) DNA-BF4; (E) DNA-BF2M1; (F) DNA-BF4M1; (G) DNA-BF2M2. The corresponding calculated molecular weight for each conjugate is presented in the figure.

VII. Assembly of the cube samples

1. Component strands of different cube samples

Each component strand was mixed in 1xPBS buffer with a final concentration of 1 μM as shown in **Table S3**. The mixture was then annealed from 95 to 4 °C in 6.5 hours.

Cube samples	Components
ssDNACb	1BA, 2HC, 3ED, 4IF
DNACb	1BA, 2HC, 3ED, 4IF, B, A, H, C, E, D, I, F
sDNACb	1BA, 2HC, 3ED, 4IF, sB, sA, sH, sC, sE, sD, sI, sF
F-DNACb	1BA, 2HC, 3ED, 4IF, Bf, Af, Hf, Cf, Ef, Df, If, Ff
DPCb	1BA, 2HC, 3ED, 4IF, B-BF2, A-BF4, H-BF2, C-BF4, E-BF3, D-BF1, I-BF3, F-BF1
rDNACb	L1, L2, L3, L4, 1H4, 2B3, 3C4, 4A3, 1E2, 2I1, 3F2, 4D1, B, A, H, C, E, D, I, F
rDPCb	L1, L2, L3, L4, 1F2, 2A3, 3C4, 4D1, 2I1, 1E4, 4H3, 3B2, D-BF1, C-BF4, E-BF3, B-BF2, H-BF2, A-BF4, I-BF3, F-BF1
NDPCb	1BA, 2HC, 3ED, 4IF, B-BF4, A-BF2, H-BF2, C-BF4, E-BF3, D-BF1, I-BF1, F-BF3
sDPCb	1BA, 2HC, 3ED, 4IF, sB-BF2, sA-BF4, sH-BF2, sC-BF4, sE-BF3, sD-BF1, sI-BF3, sF-BF1
DPCb-1 subunit	1BA, 2HC, 3ED, 4IF, D-BF1, I-BF2, H-BF3, A-BF4
DPCb-M1	1BA, 2HC, 3ED, 4IF, B-BF2M1, A-BF4M1, H-BF2M1, C-BF4M1, E-BF3, D-BF1, I-BF3, F-BF1
NDPCb-M1	1BA, 2HC, 3ED, 4IF, B-BF4M1, A-BF2M1, H-BF2M1, C-BF4M1, E-BF3, D-BF1, I-BF1, F-BF3
DPCb-M2	1BA, 2HC, 3ED, 4IF, B-BF2M2, A-BF4, H-BF2M2, C-BF4, E-BF3, D-BF1, I-BF3, F-BF1
NDPCb-M2	1BA, 2HC, 3ED, 4IF, B-BF4, A-BF2M2, H-BF2M2, C-BF4, E-BF3, D-BF1, I-BF1, F-BF3
DPCb-Overhang	1BA, 2HC, 3ED, 4IF, Bn-BF2, A-BF4, Hn-BF2, C-BF4, En-BF3, D-BF1, In-BF3, F-BF1
DPCb-1 Overhang	1BA, 2HC, 3ED, 4IF, B-BF2, A-BF4, Hn-BF2, C-BF4, E-BF3, D-BF1, I-BF3, F-BF1
NDPCb-Overhang	1BA, 2HC, 3ED, 4IF, Bn-BF4, A-BF2, Hn-BF2, C-BF4, En-BF3, D-BF1, In-BF1, F-BF3
NDPCb-1 Overhang	1BA, 2HC, 3ED, 4IF, B-BF4, A-BF2, Hn-BF2, C-BF4, E-BF3, D-BF1, I-BF1, F-BF3
DNACb-Overhang	1BA, 2HC, 3ED, 4IF, Bn, Af, Hn, Cf, En, Df, In, Ff
DNACb-1 Overhang	1BA, 2HC, 3ED, 4IF, Bf, Af, Hn, Cf, Ef, Df, If, Ff

Table S3. Component strands of different cube samples.

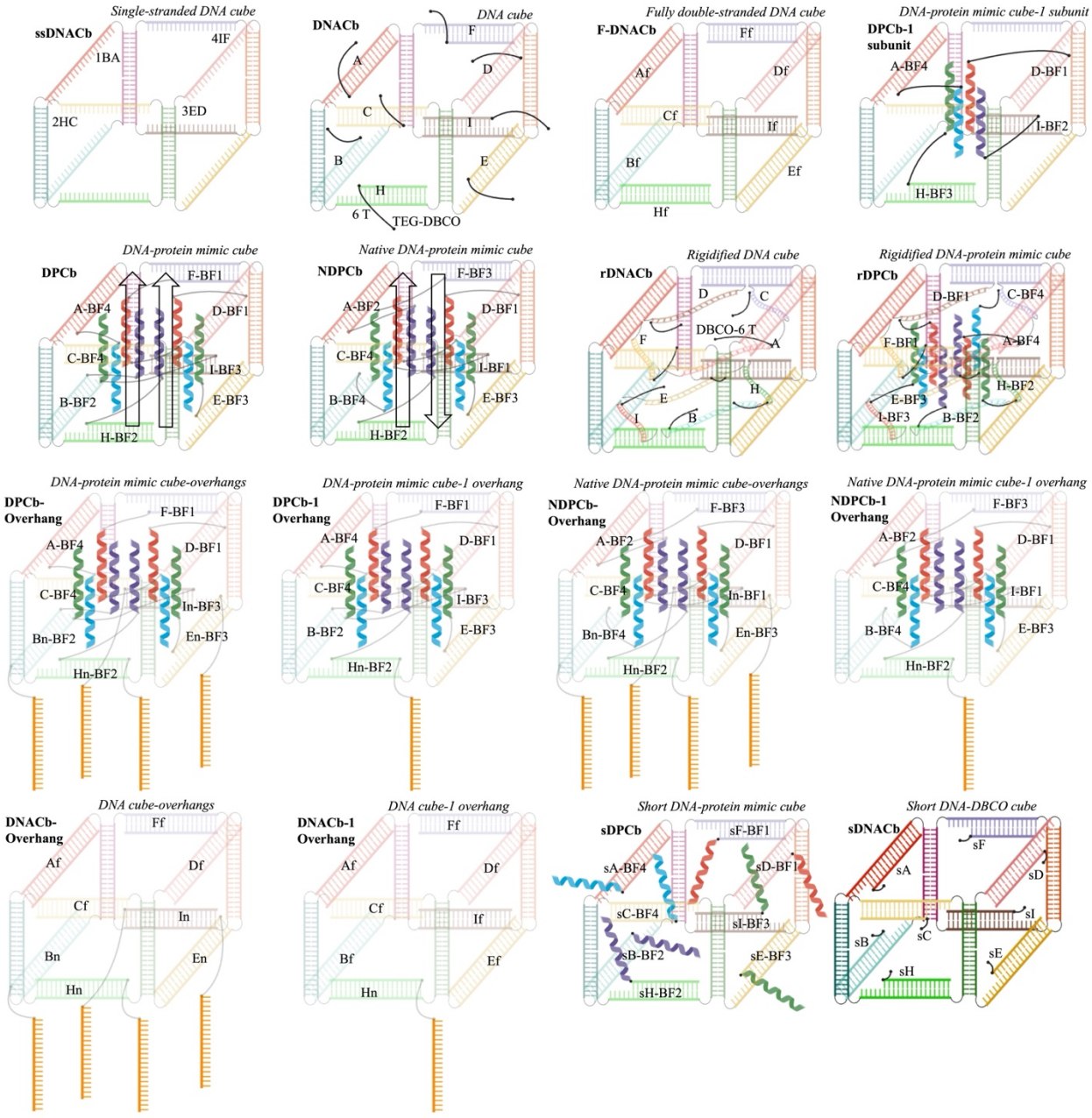

Figure S5. Schematic representation of different cubes and the spatial positions of their component strands.

2. Gel electrophoresis characterization of cube structures

The assembled cube samples were loaded onto 2% native agarose gels for characterizing the assembly.

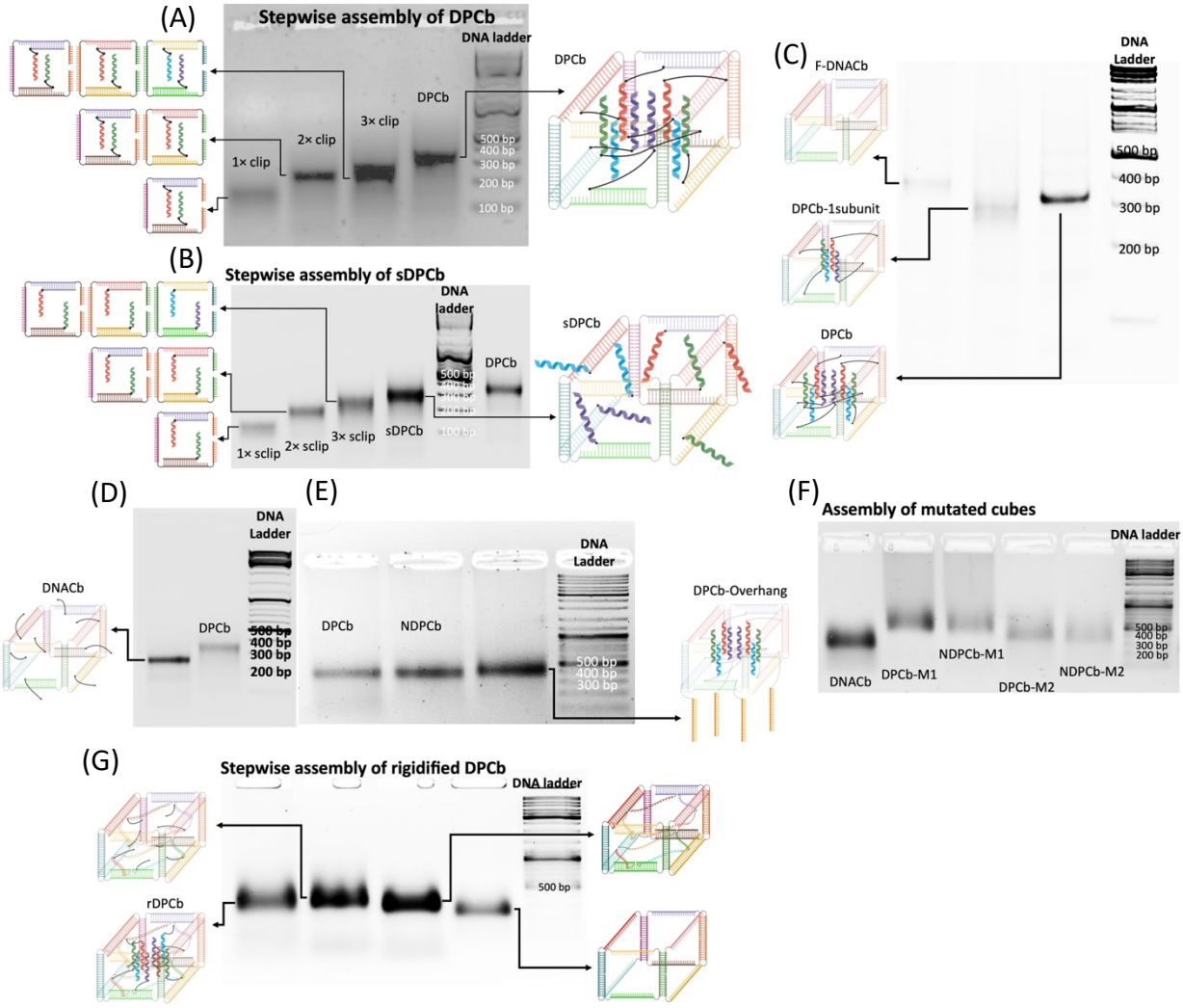

Figure S6. Assembly of all cubes used in this study. 2% native AGE was used to characterize the assembly, and GeneRuler DNA Ladder Mix was used as a reference.

3. Assembly of bacterioferritin capsule mimics

Single stranded SNA was annealed from 95 to 20 °C in 1 hour to form the spheres.[2] Cube structures featuring complementary overhangs were assembled separately, and then mixed with SNA at room temperature. The higher-order structure can be obtained within 1 minute (**Figure 6A**). Structures with different compositions can be achieved by adjusting the ratio of cube:SNA. Experiments for screening cube:SNA ratio were presented in **Figure S7** & **Figure S8**.

The assembly of cubes with two parallel subunits and SNA was studied here. Two cube samples with one or four overhang strands were assembled and mixed with SNA in different ratios. The ratio calculation was presented in two ways: 1. The number of overhang strands versus the number of single stranded SNA; 2. The number of cubes versus the number of spheres. Cubes featuring four overhangs can assemble better with SNA (Lane11, **Figure S7**) compared to cubes with only one overhang (Lane 8, **Figure S7**), owing to the enhanced cooperativity from a higher number of overhangs per cube.

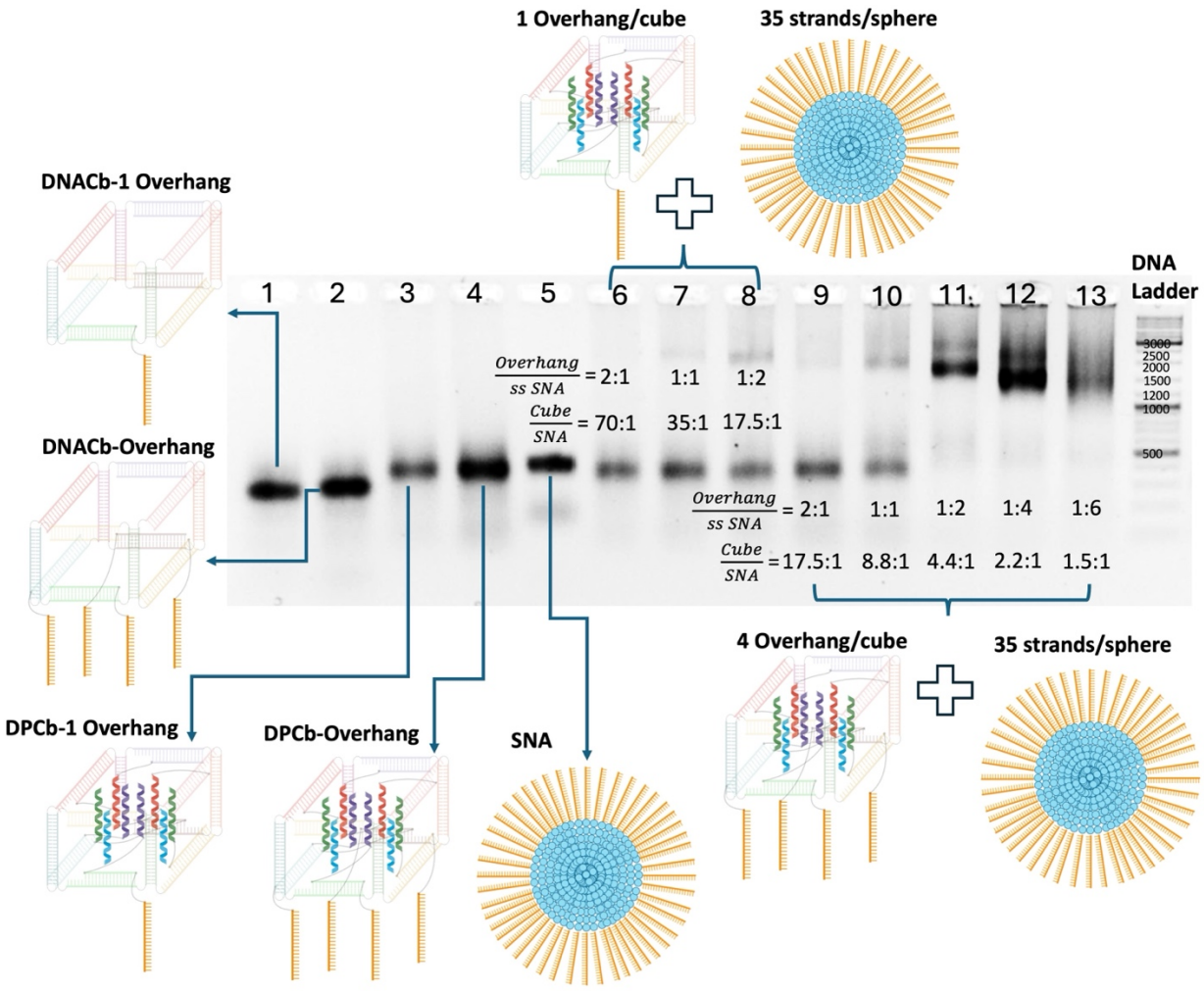

Figure S7. 2% Native AGE showing the assembly of DPCb featuring overhangs and SNA. Lane 1: DNACb-1 Overhang. Lane 2: DNACb-Overhang. Lane 3: DPCb-1 Overhang. Lane 4: DPCb-Overhang. Lane 5: SNA. DPCb-1 Overhang + SNA were loaded on Lane 6 (overhang/ss SNA = 2:1), Lane 7 (overhang/ss SNA = 1:1) and Lane 8 (overhang/ss SNA = 1:2). DPCb-Overhang + SNA was loaded on Lane 9 (overhang/ss SNA = 2:1), Lane 10 (overhang/ss SNA = 1:1), Lane 11 (overhang/ss SNA = 1:2), Lane 12 (overhang/ss SNA = 1:4), and Lane 13 (overhang/ss SNA = 1:6). Cube final concentration after mixing is 0.5 µM for all samples. GeneRuler DNA Ladder Mix was used in this study.

The assembly of cubes with two antiparallel subunits and SNA was also studied. Similar results were observed (**Figure S8**) since this higher-order assembly is governed by DNA scaffolds.

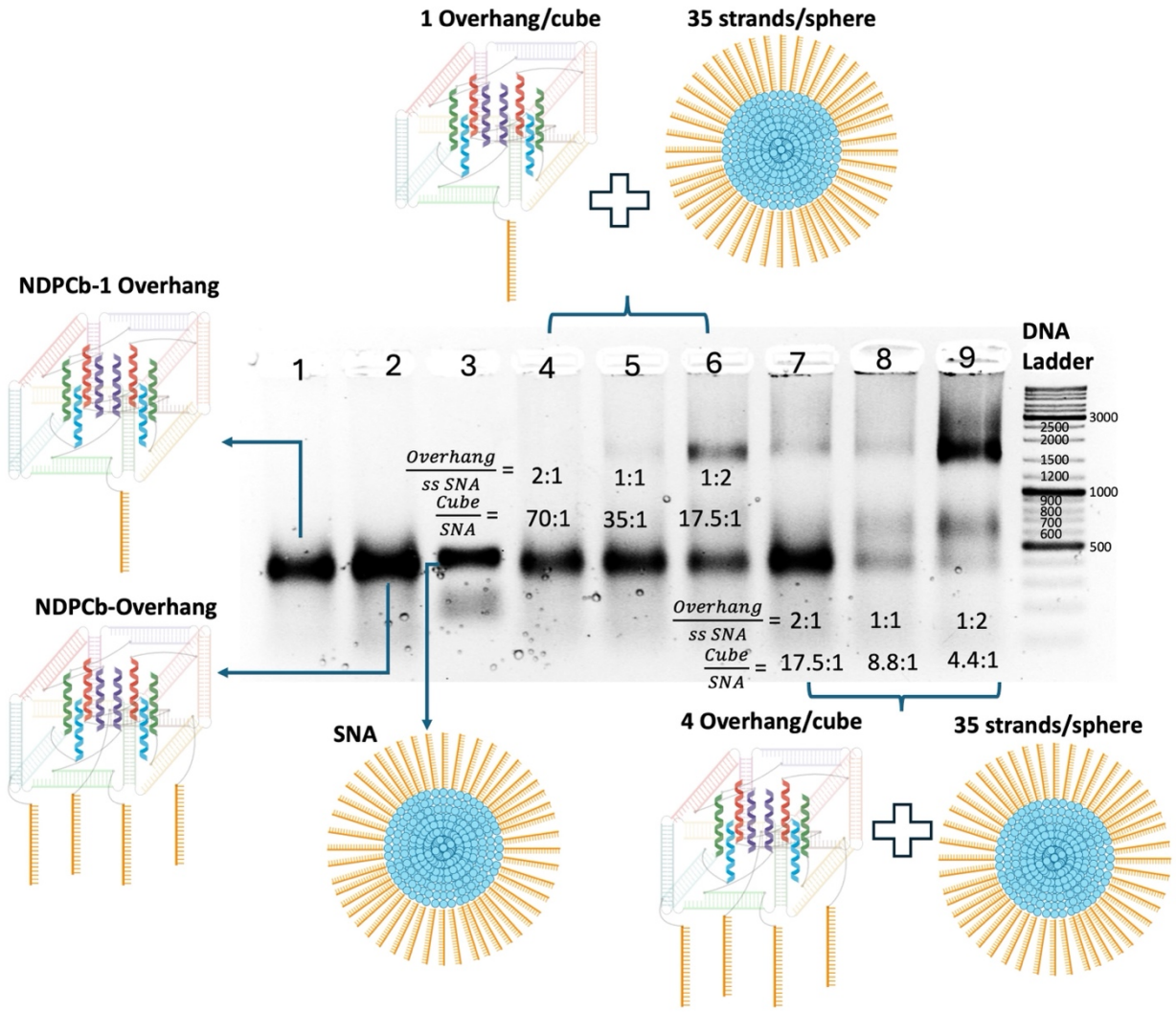

Figure S8. 2% Native AGE showing the assembly of NDPCb featuring overhangs and SNA. Lane 1: NDPCb-1 Overhang. Lane 2: NDPCb-Overhang. Lane 3: SNA. NDPCb-1 Overhang + SNA were loaded on Lane 4 (overhang/ss SNA = 2:1), Lane 5 (overhang/ss SNA = 1:1) and Lane 6 (overhang/ss SNA = 1:2). NDPCb-Overhang + SNA was loaded on Lane 7 (overhang/ss SNA = 2:1), Lane 8 (overhang/ss SNA = 1:1), and Lane 9 (overhang/ss SNA = 1:2). Cube final concentration after mixing is 0.5 μM for all samples. GeneRuler DNA Ladder Mix was used in this study.

4. Strand displacement of DPCb

To obtain the cube with varying numbers of DNA-peptide conjugates, DPCb was first prepared as described in **SI-VII-1**. The cube sample was then transferred to a pre-dried Eppendorf tube

containing 2 equivalents of the displacing strands (see **Table S4**). The mixture was equilibrated for 20 mins at room temperature. A native PAGE was then used to check the displaced cube samples (**Figure 5B**).

Displacement	Number of peptides per cube	Displacing strands added
Displacing 1 strand	7	Af
Displacing 2 strands	6	Af, Bf
Displacing 3 strands	5	Af, Bf, If
Displacing 4 strands	4	Af, Bf, If, Ff
Displacing 5 strands	3	Af, Bf, If, Ff, Cf
Displacing 6 strands	2	Af, Bf, If, Ff, Cf, Hf
Displacing 7 strands	1	Af, Bf, If, Ff, Cf, Hf, Df
Displacing 8 strands	0	Af, Bf, If, Ff, Cf, Hf, Df, Ef

Table S4. DNA strand components for the displacement of DPCb.

VIII. AFM images of the cube samples

In this study, all structures were assembled in 1xTAMg buffer at 1 μM concentration. For DPCb with heme, 10 eq of ferroheme were added to cube samples and equilibrated for 30 mins at room temperature for ligand binding. For samples with iron, 50 eq of $FeSO_4$ were added to cube samples, followed by the addition of 50 eq of H_2O_2 to promote oxidation. All samples were diluted to 50 nM before loading on AFM tips. Peptide particles were assembled using 150 μM of each BF1-4.

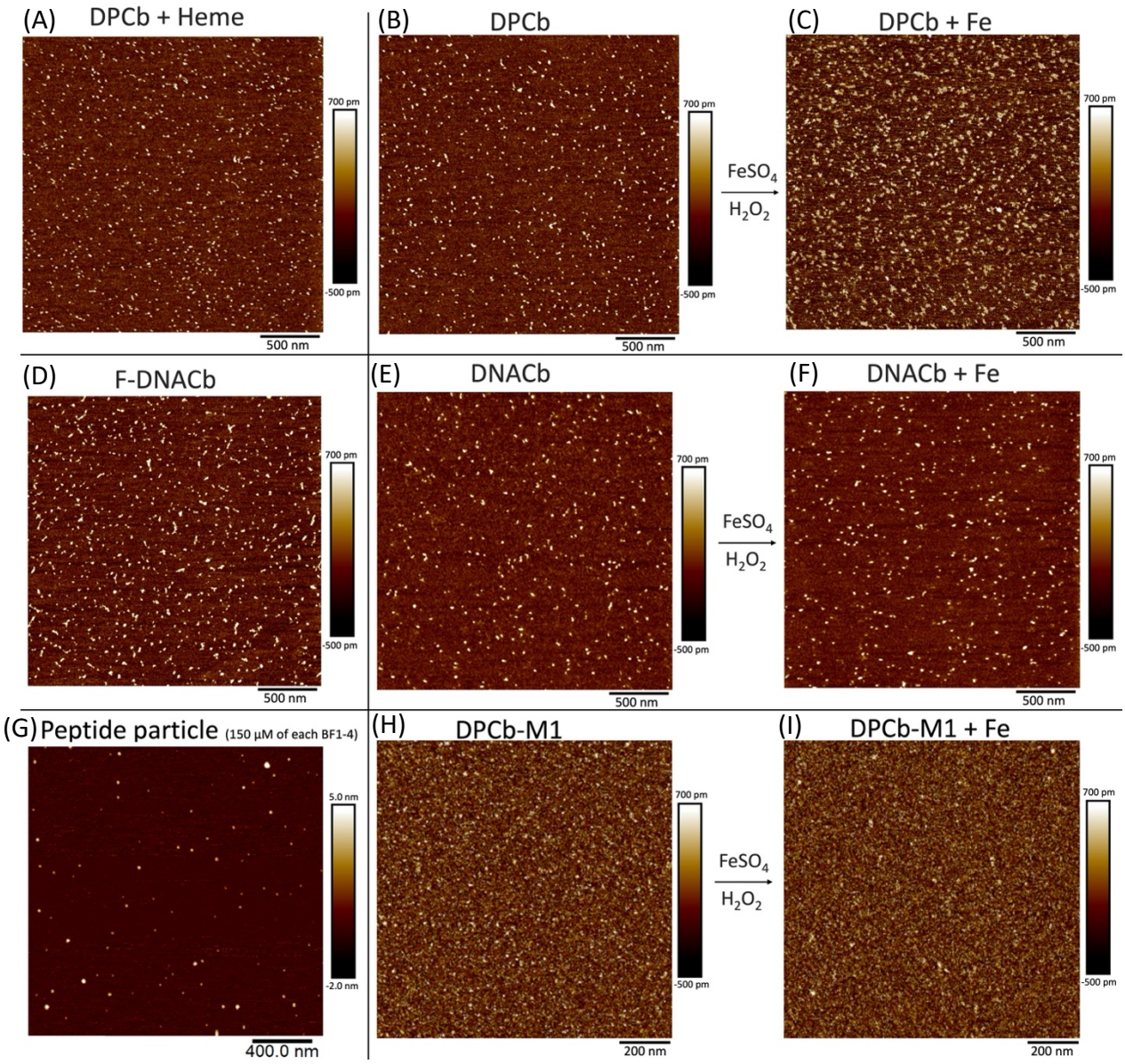

Figure S9. AFM images of cube samples. (A) DPCb with heme. (B) DPCb. (C) DPCb after iron oxidation. (D) Cube hybridized to fully complementary strands (F-DNACb). (E) DNACb. (F) DNACb after iron oxidation. (G) Peptide particle. (H) DPCb-M1. (I) DPCb-M1 after iron oxidation.

The AFM images of higher-order structures assembled from cube and SNA are represented here. All cube samples were assembled and mixed with SNA with a final concentration of 0.5 µM. The mixtures were then diluted to 50 nM before loading on AFM tips. Additional DLS characterisation of cube-SNA complex with varying cube/SNA ratios were provided in **Figure S22**.

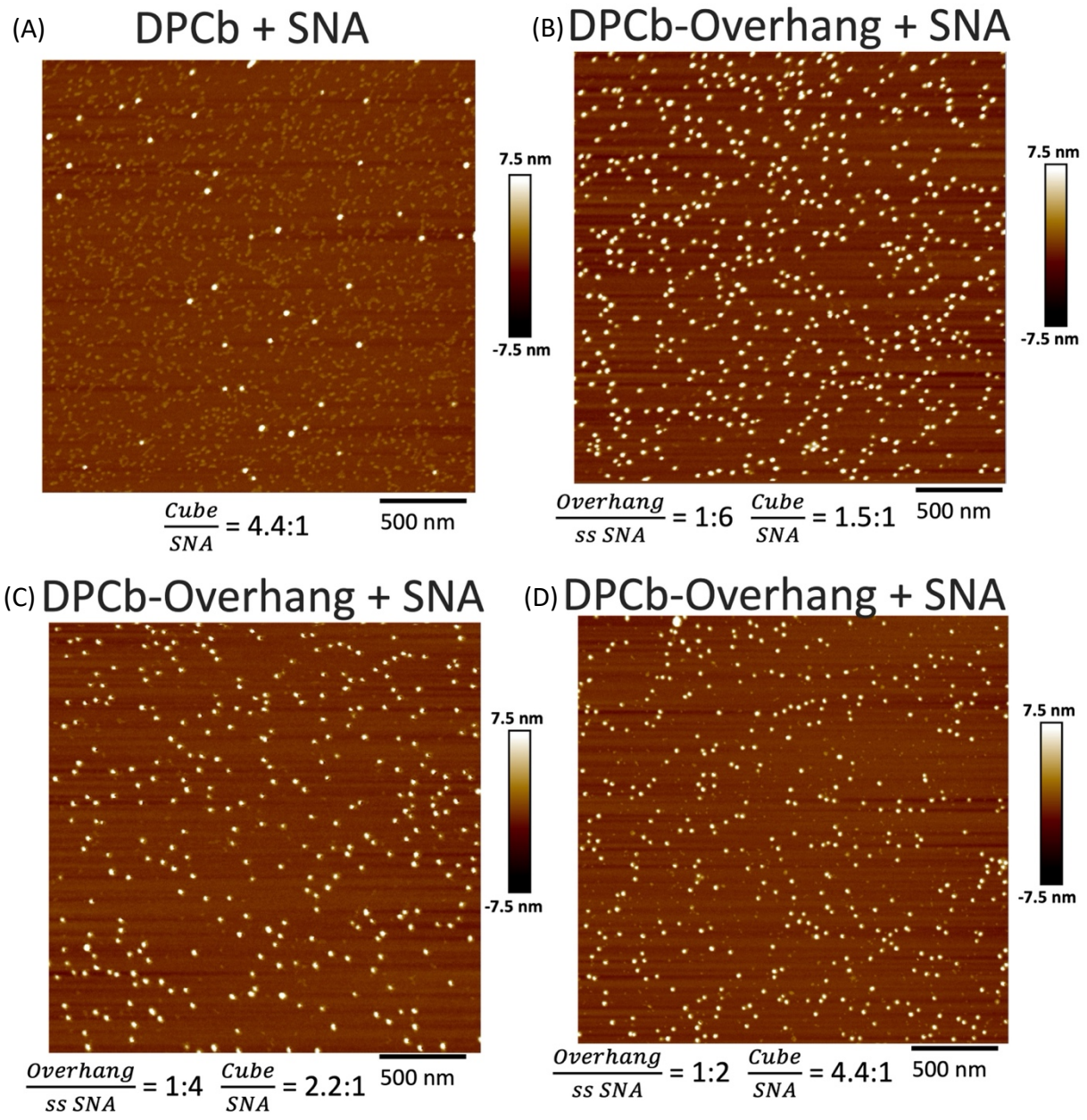

Figure S10. AFM images of cube samples mixed with SNA. (A) DPCb + SNA. (B-D) DPCb-Overhang + SNA with varying ratios.

IX. Circular dichroism spectroscopy characterization

1. CD spectra of peptide solutions

CD spectroscopy was applied to study the conformation of non-scaffolded peptide mixtures. Peptide BF1-4 were first prepared at 50 μM each (total peptide concentration: 200 μM) in 1xNaF buffer to get a clean background signal in the short wavelength region (**Figure S11A**, blue line). $FeSO_4$ was added to a final concentration of 250 μM (2.5 eq to iron sites) to probe potential conformational changes (**Figure S11A**, orange line). Both spectra exhibited a negative maximum at around 201 nm.

To assess concentration effects on non-scaffolded assembly, the peptides were assembled at 150 μM each (total peptide concentration: 600 μM) in 1xNaF buffer (**Figure S11B**, blue line). Metal-peptide complex was prepared by adding $FeSO_4$ to a final concentration of 750 μM (2.5 eq to iron sites) (**Figure S11B**, orange line). At this higher concentration, peptide solutions displayed negative maxima near 205 nm, suggesting a more structured conformation.

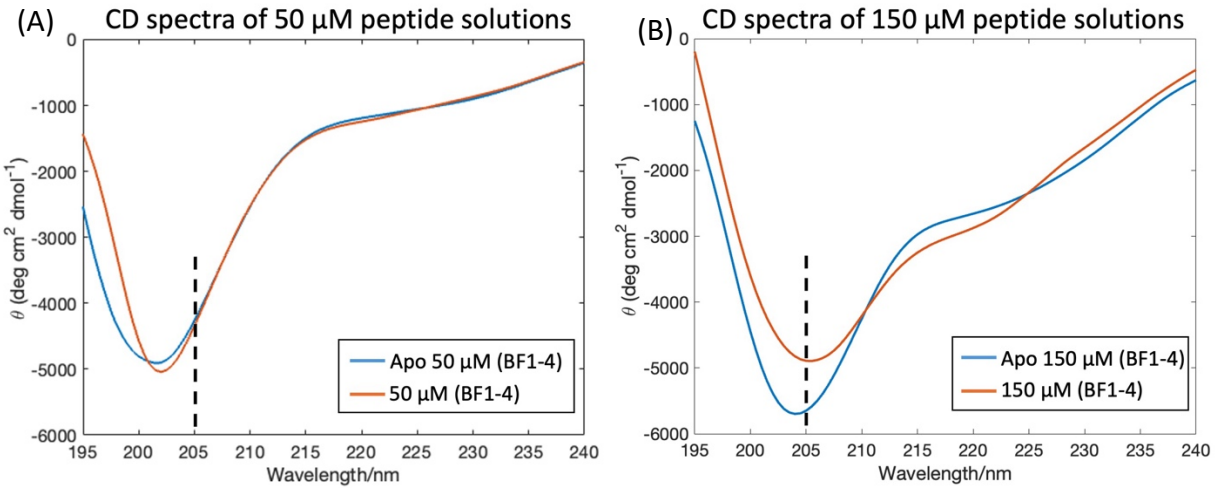

Figure S11. (A) CD spectra of 50 μM (BF1-4). (B) CD spectra of 150 μM (BF1-4).

2. CD spectra of cube constructs

Cube constructs were assembled in 1xNaF buffer to get a clean background in the short wavelength region on CD spectra. The final concentration of assembled structures for CD study is 1 μM. Samples were annealed from 95 to 4 °C in 6.5 hours. $FeSO_4$ was then added to the samples (final concentration: 10 μM). Afterwards, CD spectroscopy was employed to characterize the structures (**Figure S12**). To isolate the peptide conformation spectra, DNA scaffold samples were prepared and scanned following the same procedure, and their CD spectra were subtracted as backgrounds.

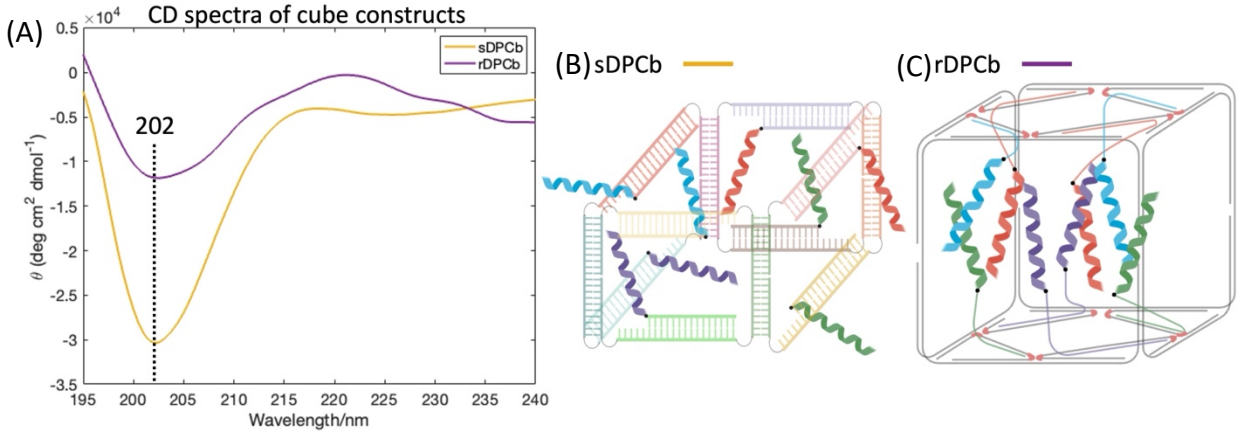

Figure S12. (A) CD spectra of sDPCb and rDPCb ([Cube] = 1 μM; [$FeSO_4$] = 10 μM). (B) Schematic representation of sDPCb. (C) Schematic representation of rDPCb.

3. CD spectra of cubes with varying sequences and subunit orientations

AlphaFold predictions of the original and Mutant 1 subunits are shown in **Figure S13A&B**, respectively. CD spectra of cubes containing two parallel subunits are presented in **Figure S13C&D**, while spectra of cubes with two antiparallel subunits are shown in **Figure S13E&F**. Apo samples were measured at 1 μM construct concentration in 1xNaF buffer. Metal-cubes were measured at 1 μM construct in 1xNaF buffer with 10 μM $FeSO_4$.

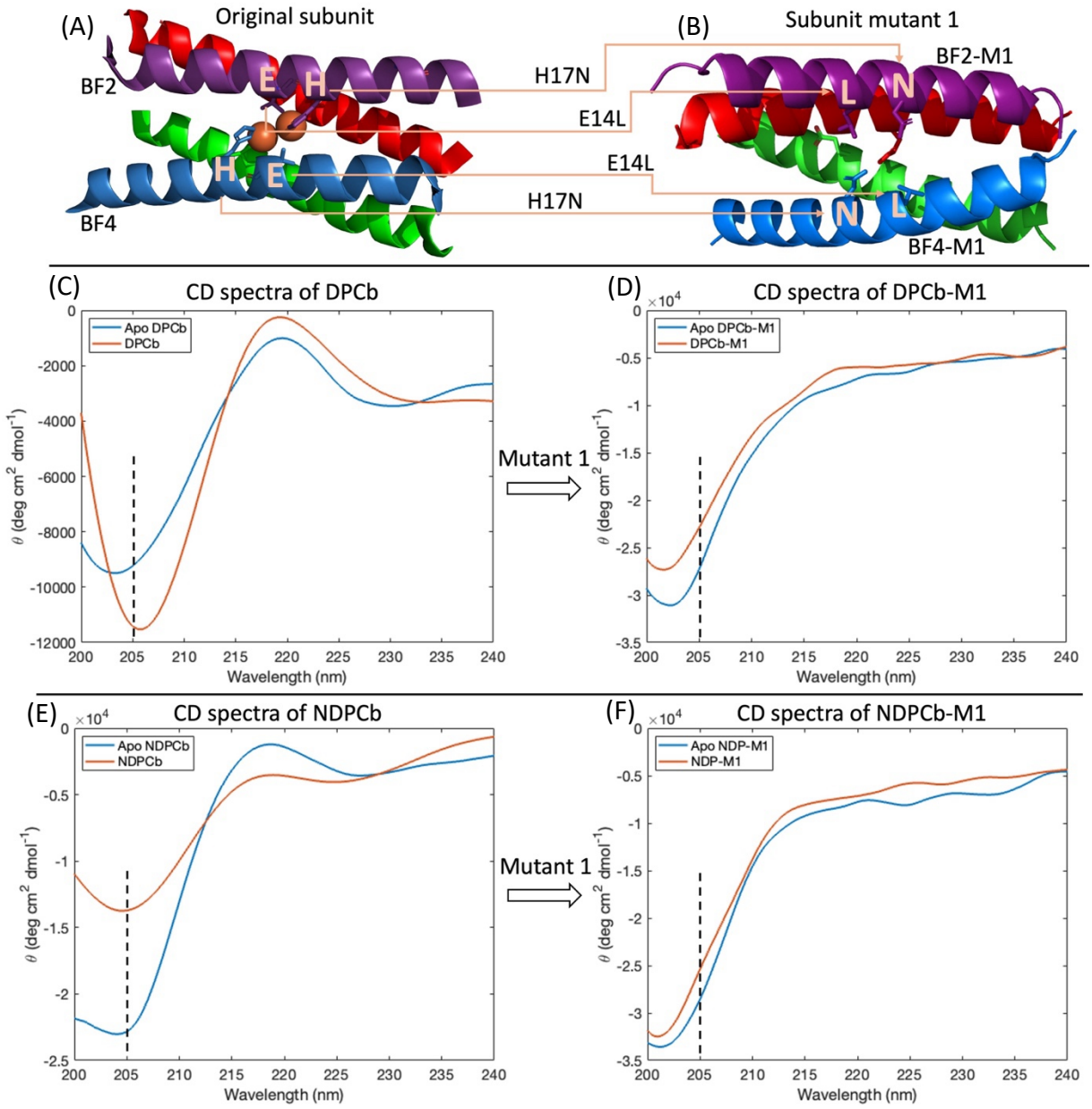

Figure S13. (A) AlphaFold prediction of one original subunit. (B) AlphaFold prediction of one subunit Mutant 1. (C) CD spectra of DPCb. (D) CD spectra of DPCb-M1. (E) CD spectra of NDPCb. (F) CD spectra of NDPCb-M1.

X. Thermal denaturation study

Cube structures were assembled at 1 μM in 1xPBS buffer. Then UV-260 melting study was performed on the samples with 2 °C/minute ramping rate. UV-260 melting curves of ssDNACb

and DNACb were shown in **Figure S14A**, and their first derivatives were shown in **Figure S14B**. First derivative of UV-260 melting results and DPCb and NDPCb were shown in **Figure S14C**. The UV-260 melting curve of rDPCb was shown in **Figure S14D**, where a two-stage melting pattern was observed due to the presence of splint strands within the cube scaffold.

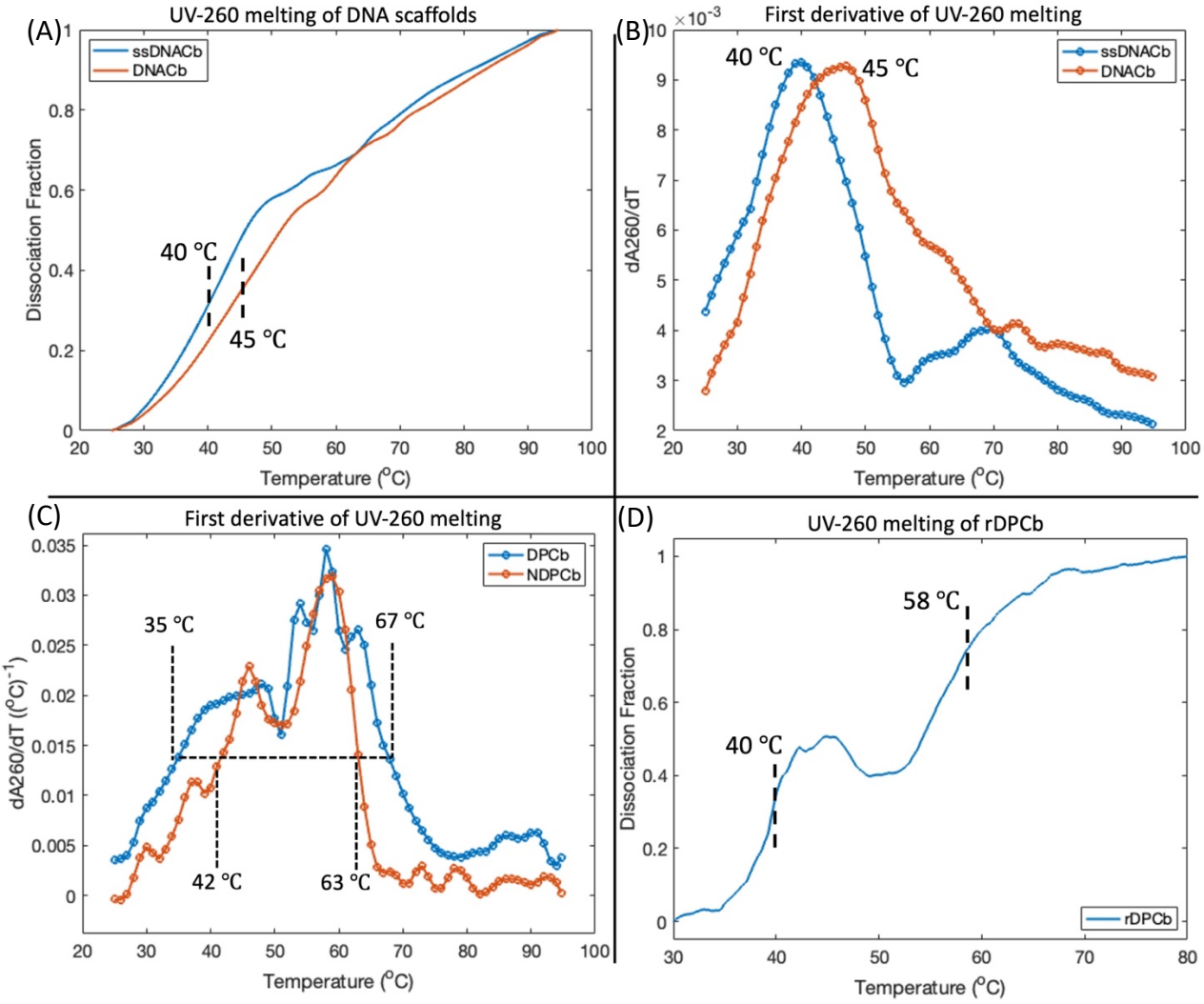

Figure S14. Thermal stability of different DNA cube-protein mimics. (A) UV-260 melting curves of ssDNACb and DNACb. (B) First derivatives of UV-260 signals of ssDNACb and DNACb. (C) First derivative of UV-260 melting study of DPCb and NDPCb. (D) UV-260 melting of rDPCb.

XI. Biophysical parameter determination

1. Heme binding and thermal releasing

To determine the cube-ferroheme dissociation constant K_D, a titration assay was carried out by adding DPCb to ferroheme solution (**Figure S15A**). The apparent Soret band peak at 389 nm was followed to track the binding process. Values were calculated by using the equations described below:[3, 4]

$$[S] = [S_u] + [SH], [H] = [H_u] + [SH]$$

$$K_D = \frac{[S_u][H_u]}{[SH]} = \frac{([S] - [SH])([H] - [SH])}{[SH]}$$

$$K_D[SH] = ([S] - [SH])([H] - [SH])$$

$$[SH]^2 - [H][SH] - [S][SH] - K_D[SH] + [S][H] = 0$$

$$[SH] = \frac{([S] + [H] + K_D) \pm \sqrt{([S] + [H] + K_D)^2 - 4[S][H]}}{2}$$

$$A389 = \varepsilon_1[H_u]l + \varepsilon_2[SH]l = \varepsilon_1([H] - [SH])l + \varepsilon_2([SH])l$$

$$A389 = \varepsilon_1[H]l + \frac{(\varepsilon 2 - \varepsilon 1)l}{2} \times (([S] + [H] + K_D) - \sqrt{([S] + [H] + K_D)^2 - 4[S][H]})$$

In this equation, [S] denotes the total concentration of cube sample, $[S_u]$ the concentration of unbound sample, [H] the total concentration of ferroheme, $[H_u]$ the concentration of unbound ferroheme, [SH] the concentration of sample-ferroheme complex, and K_D the dissociation constant of the complex. The negative root of the quadratic solution is physically relevant. ε_1 is the extinction coefficient of unbound ferroheme at 389 nm, and ε_2 is the extinction coefficient of

sample-ferroheme complex at 389 nm. As shown in **Figure S15B**, DPCb binds heme with a submicromolar dissociation constant.

The UV-vis spectra of heme binding suggested that NDPCb has different binding behavior compared to DPCb (**Figure 4C** & **Figure S16**). To further prove the heme binding in NDPCb, we assembled NDPCb-M2 by mutating the Met residue to Leu at the proposed binding site (**Table S3**). As shown in **Figure S15C**, NDPCb-M2 exhibited a decrease in signal intensity, which is similar to the trend observed for DPCb and DPCb-M2 (**Figure 3H**). It is noted that DPCb-M2 still has higher absorbance around 400 nm compared to DNACb with heme, likely due to non-specific peptide-heme interactions. To further distinguish specific and nonspecific binding, we performed thermal release experiments (**Figure S15D**). Monitoring absorbance at 400 nm as a function of temperature revealed that NDPCb-heme exhibited a decreasing trend with fluctuations within the DNA melting temperature range. In contrast, NDPCb-M2 showed an increasing trend. These patterns are consistent with those observed for DPCb and DPCb-M2 (**Figure 3J**). In addition, we compared the full UV-vis spectra of native and thermally denatured cube-heme complexes. Cubes were mixed with heme equimolarly (cube: heme = 1:1 μM). As shown in **Figure S15E**, blue lines represent UV-vis spectra obtained at room temperature, while red lines represent spectra of denatured samples after 10 minutes incubation at 85 °C. DPCb (solid line) and NDPCb (dotted line) with heme binding pockets exhibited absorbance decrease in the Soret region after heating. By contrast, without the scaffolded binding pocket, heme with DNACb and peptide mixture (circle) displayed an increase. Difference spectra (native minus denatured) are shown in **Figure 15F**. Both DPCb and NDPCb display maxima at 417 nm, which match the Soret peak position of native Bfr-heme.[5]

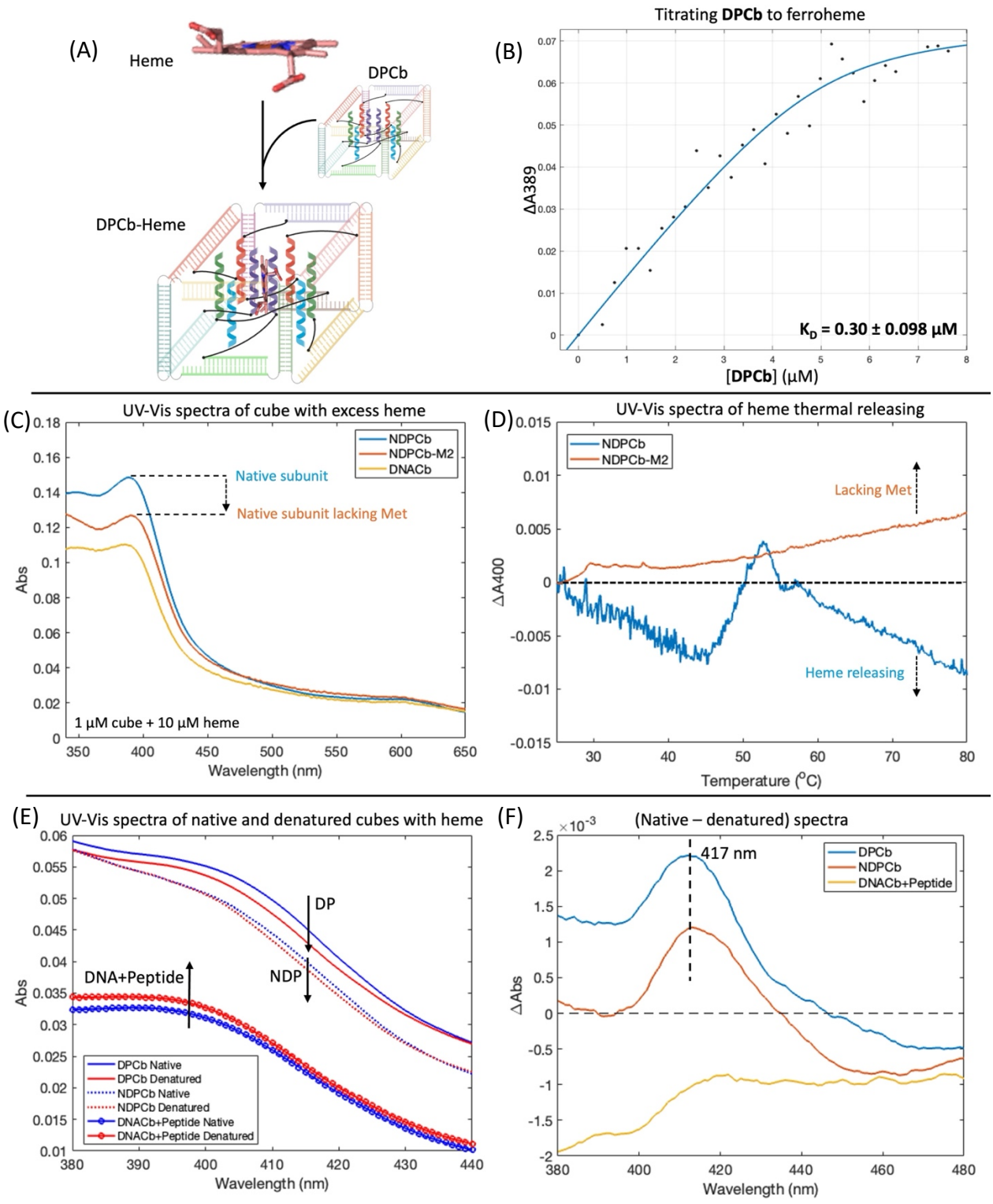

Figure S15. (A) Schematic representation of the UV-vis titration experiment, in which DPCb solution was incrementally added to heme solution. (B) Fitted results of DPCb-heme titration experiment. Errors represent fitting uncertainties obtained from data analysis in MATLAB using the described equations. (C) UV-vis spectra of 1 μM cube with 10 μM heme at room temperature. (D) Abs400-melting study of NDPCb-heme and NDPCb-M2-heme. (E) UV-vis spectra of 1 μM

cube with 1 μM heme measured at room temperature (native) and 85 °C (denatured). (F) Difference spectra calculated by subtracting the denatured spectrum from the native spectrum.

To examine the heme binding properties of cube with different subunit orientations, DPCb and NDPCb were mixed with varying amounts of heme and analyzed by UV-vis spectroscopy. Measurements were performed under two conditions. In the saturated heme condition, excess cube constructs were mixed with a limited amount of heme (**Figure S16A**; final cube concentration = 5 μM). In the saturated cube condition, heme was present in excess relative to the cube constructs (**Figure S16B**; final cube concentration = 1 μM). In all cases, spectra of the corresponding apo cubes without heme were subtracted as background to isolate the heme associated signals.

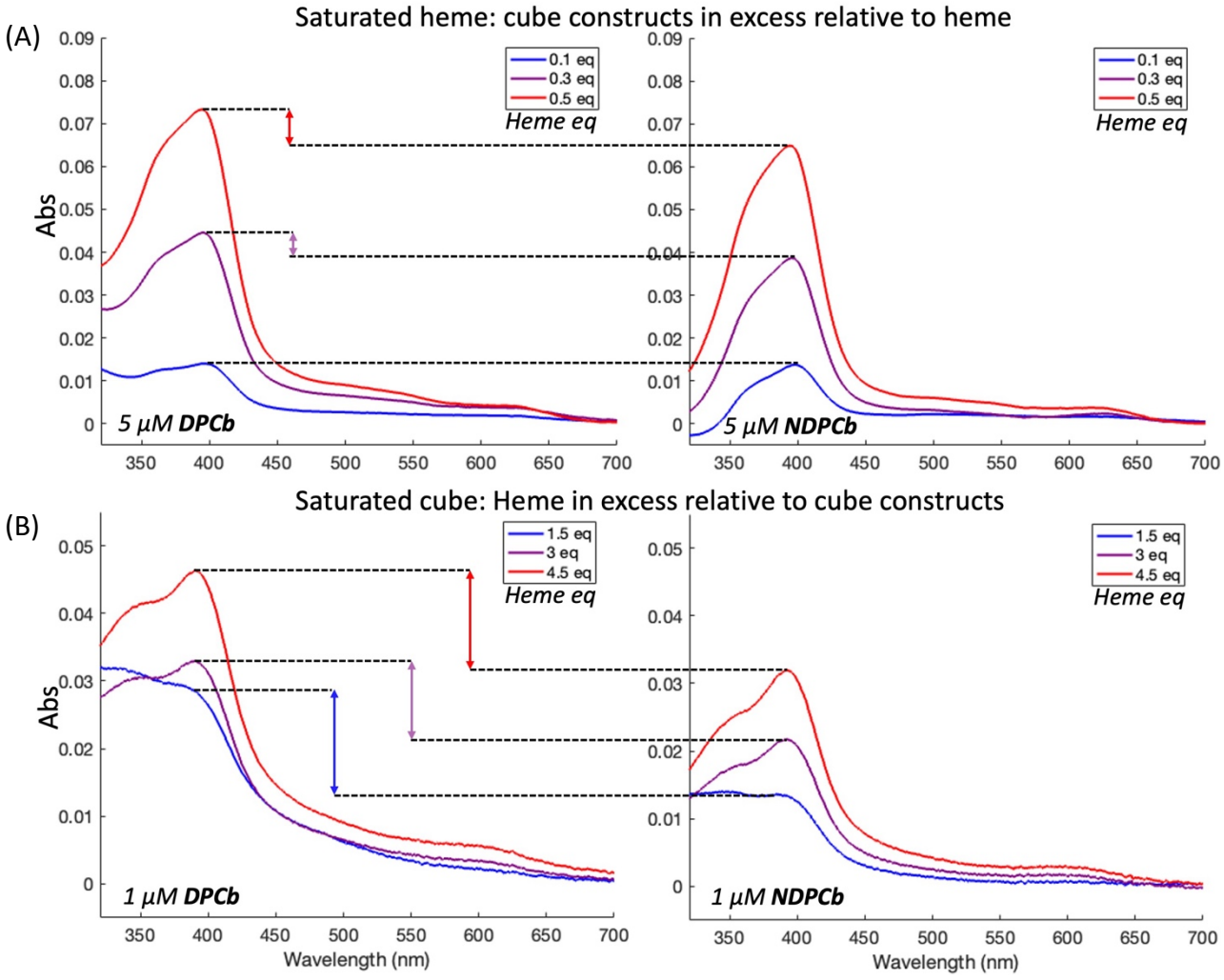

Figure S16. UV-vis spectra of cube-heme under different binding conditions. (A) Spectra of 5 μM cube constructs mixed with a limited amount of heme. (B) Spectra of 1 μM cube constructs mixed with excess heme.

2. Iron oxidation

To determine the iron oxidation ability spectroscopically, cube constructs were first mixed with excessive heme (cube: ferroheme = 1:10 μM) in oxygenated 1xPBS buffer. Different amount of $FeSO_4$ was then added to the mixture. Spectra were collected after 10 minutes of equilibration (**Figure 4C**). To determine the kinetic parameters of iron oxidation, cube-protein mimic samples were assembled in 1xPBS, then buffer exchanged into a deoxygenated 1xMES buffer (100mM MES, 130 mM NaCl, pH = 6.5). $FeSO_4$ was then added to cube samples anaerobically to minimize the interference from dissolved O_2. The mixture was mixed with H_2O_2 solutions in a stopped-flow manner. The oxidation process was monitored by a UV-vis spectrometer at 340 nm. Exemplary kinetic plots of iron oxidation by DPCb, and DPCb-SNA were shown in **Figure S17A**. The raw data were fitted using a two-exponent function:[6]

$$\Delta A = a \times e^{-kfast*t} + b \times e^{-kslow*t}$$

This comprises a fast process and a slow process. The dominant $kfast$ is the pseudo-first-order rate constant corresponding to the fast process (**Figure S17B**).

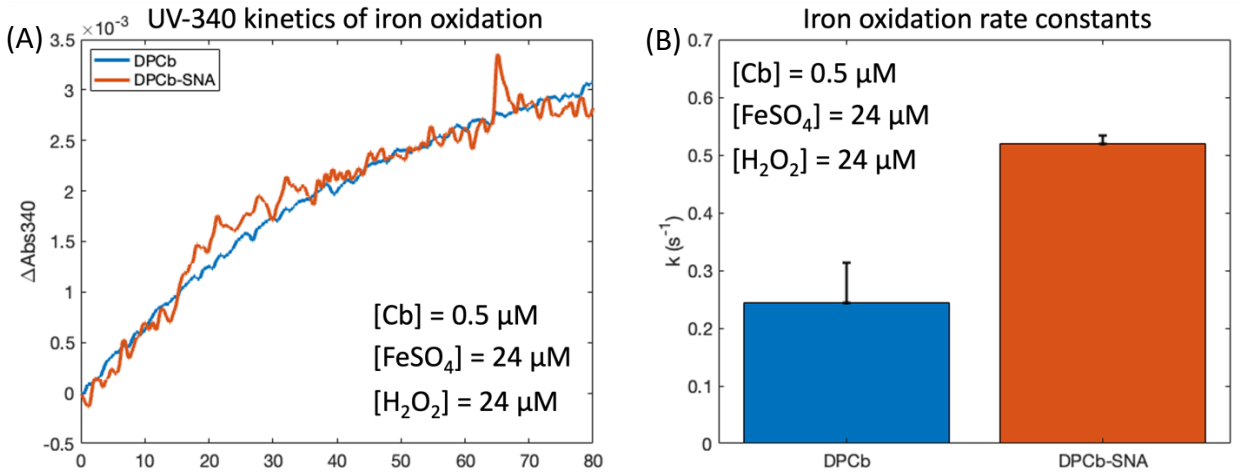

Figure S17. Iron oxidation kinetic parameters of different DNA cube-protein mimics. (A) Exemplary Fe(II) oxidation plots by different constructs using H_2O_2. (B) The resulting *kfast* values of these experiments. Each spectra comprises three replicas.

Iron oxidations were performed on DPCb with varying H_2O_2 concentrations to determine the kinetic parameters. The final DPCb concentration is 1 μM and the final $FeSO_4$ concentration is 48 μM. Experiments with final H_2O_2 concentrations of 48, 72, 96, 120, and 144 μM were carried out (**Figure S18A**). The *kfast* values were determined by the previously described data fitting model, and linearly related to [H_2O_2] (**Figure S18B**). This linear relationship aligns with reported natural Bfr patterns.[6]

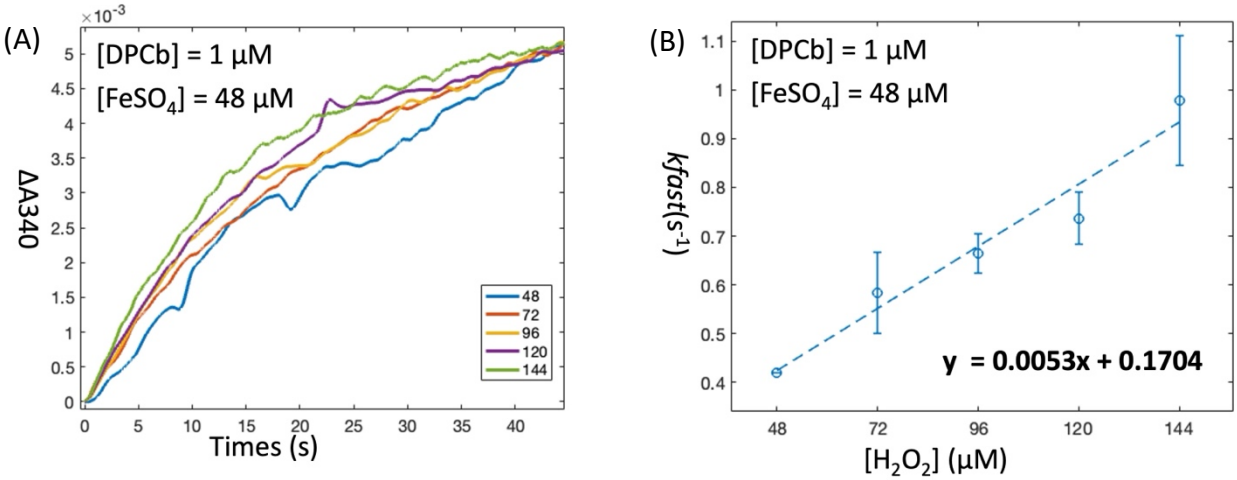

Figure S18. Iron oxidation kinetic parameters of DPCb. (A) Five exemplary UV-340 kinetics of iron oxidation by DPCb using H_2O_2 at varying concentrations. (B) The resulting *kfast* values are linearly related to [H_2O_2]. Each measurement was repeated 2-3 times.

XII. Semiquinone radical stabilization

To examine the cube's functionality for stabilizing the semiquinone radical, 1 eq of DPCb was first assembled in 1xPBS buffer and then incubated with 50 eq $ZnSO_4$ for 30 mins at room temperature. Afterwards, a solution of Q/QH_2 was added to the cube sample. The final concentrations are as follow: $[DPCb]_f$ = 3 μM, $[Q] = [QH_2]_f$ = 10 μM.

Cube with different numbers of peptides were prepared by adding 2 eq fully complementary DNA strands to DPCb (**Figure 5A**). After strand displacement, radical stabilization experiments were performed on different cubes. Reaction process was monitored by Abs-415 kinetics (**Figure S19A**). The dA415/dT values reflecting overall reaction rates were shown in **Figure 5E**. DPCb-M1 lacking metal binding site was assembled and mixed with reactants as a control. As shown in **Figure S19B**, it exhibited the same trend as reactants in buffer.

The reaction can be carried out alternatively. DPCb full structure was first assembled and mixed with Zn^{2+} and reactants. After the first stage of reaction, fully complementary strands were added to the mixture to displace DNA-peptide conjugates. The Abs-415 kinetic measurements were resumed after 20 mins' incubation at room temperature for equilibration (**Figure 5D**). Overall substrate conversion rates were reflected by dA415/dT (**Figure S19C**). Abs-740 kinetics were carried out to reveal product formation and dissociation by displacement (**Figure S19D**).

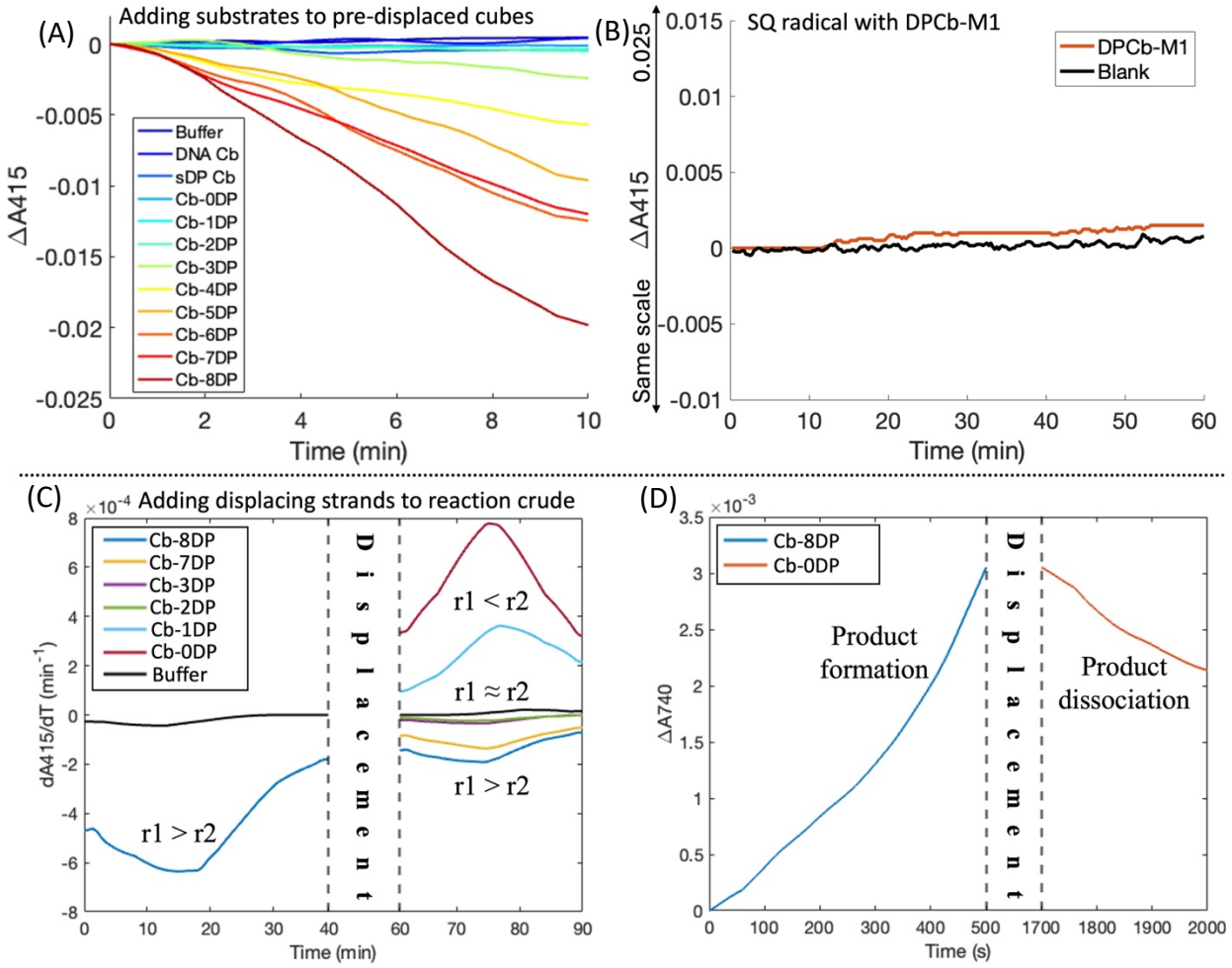

Figure S19. Semiquinone radical stabilization. (A) Schematic representation of the reversible reaction process involving helix bundle-stabilized semiquinone species. (B) Abs-415 change over time. Cubes with different number of peptides were first prepared by strand displacement. Small molecule substrates were subsequently added to cubes. (C) Abs-415 kinetics of small molecules substrates mixed with DPCb-M1 (orange) and in buffer (black) only. Plots were presented using the same y-axis scale as (B) for comparison. (D) Substrate conversion/regeneration rate represented by the derivative dA415/dT, where displacing DNA strands were introduced to pre-reacted substrates-DPCb (Cb-8DP) at the 40th minute. (D) Abs-740 kinetic plot, reflecting product formation and dissociation over time.

XIII. Cryo-EM characterization

Cryogenic electron microscopy (cryo-EM) imaging was performed on three cube assemblies: (A) DNACb, featuring flexible spacers; (B) DPCb, comprising two parallel peptide subunits without ligands; (C) NDPCb**,** incorporating two antiparallel subunits with ligands. DNACb and DPCb

constructs were imaged at a concentration of 250 nM, while NDPCb was imaged at a concentration of 350 nM. DNACb, lacking peptide fragments, was assembled in 1xTAMg. DPCb and NDPCb were assembled in 1xPBS. For ligand binding, 10 eq of $FeSO_4$ and ferroheme were added to pre-assembled NDPCb, followed by four rounds of buffer exchange against 1xPBS using Amicon3K filters to remove unbound ligands. Detailed cube compositions are provided in **Table S3** and **Figure S5**.

Cryo-EM grids of DNACb and NDPCb were prepared by applying 3 µL of sample onto negative glow-discharged holey carbon grids (CF-2/1- 3CU) and vitrified in liquid ethane using a FEI Vitrobot Mark IV system (Thermo Fisher Scientific) with the chamber set at 4 °C and 100% humidity. The blotting and plunge freezing conditions were 1.5 s (blot time), +3 (blot force), and no wait or drain time. Cryo-EM grids of DPCb were prepared identically, but 0.005% Tween20 was added to the solution prior to depositing the sample onto grids. Datasets were collected using SerialEM software,[7] in a Titan Krios microscope operated at 300 kV and equipped with a Gatan BioQuantum LS K3 electron detector. Images were collected in counting mode according to the parameters described in (**Table S5**, **Figures 4** and **S20**).

Data collection	DNACb	DPCb	NDPCb
Microscope	Titan Krios	Titan Krios	Titan Krios
Detector	Gatan BioQuantum LS K3	Gatan BioQuantum LS K3	Gatan BioQuantum LS K3
Nominal Magnification	130,000x	130,000x	130,000x
Voltage (kV)	300	300	300
Total exposure ($e^-/Å^2$)	80	80	80

Number of frames	40	40	40
Defocus range (μm)	-1.46 – -2.73	-1.26 – -3.3	-0.84 – -2.75
Calibrated physical pixel size (Å/px)	0.675	0.675	0.675
Number of movies	594	8,370	21,623
Number of particles	4,950	21,695	115,701

Table S5. Cryo-EM data collection parameters.

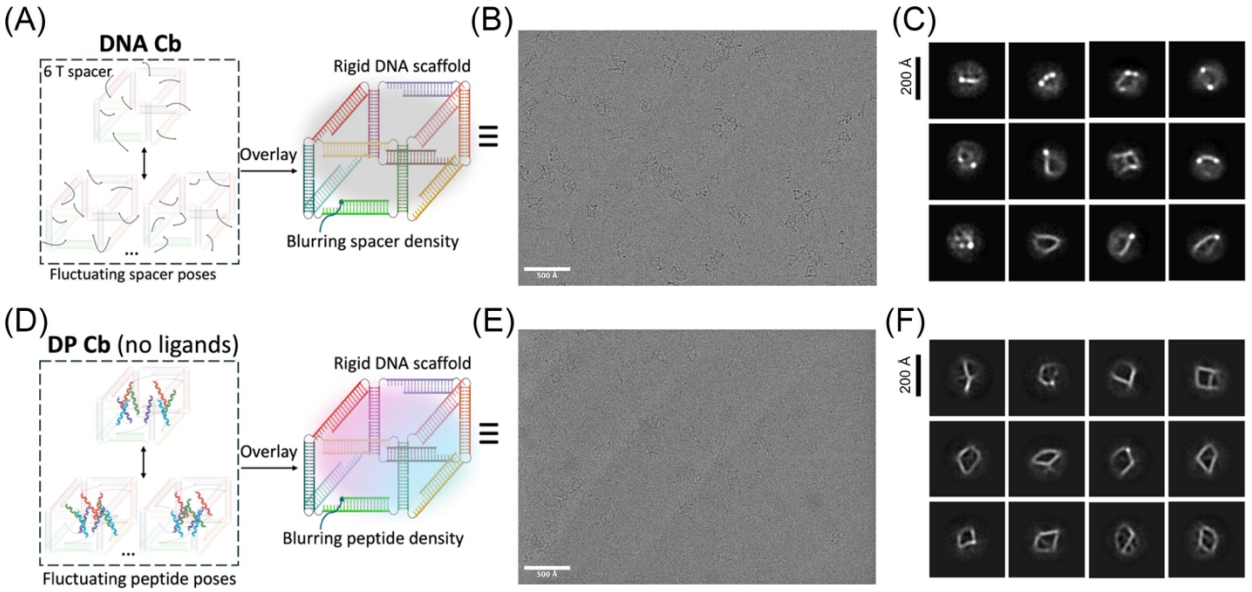

Figure S20. Cryo-EM characterization of the DNACb and DPCb (without ligands) constructs. Schematics of DNACb with single-stranded spacers but no peptides (A) and DPCb containing two parallel peptide subunits without ligands (D). Representative cryo-EM images and 2D class averages for DNACb (B, C) and DPCb (E, F).

All cryo-EM data processing steps were performed using CryoSPARC v4.1.1.[8] Movies were corrected for beam-induced motion using Patch Motion Correction with default settings. All frames in the movies were used to produce merged micrographs. The Contrast Transfer Function (CTF) parameters were estimated using the Patch CTF estimation using default settings. About 1000 particles were manually picked and extracted at either box size 582 (DNACb) or 588 pixels

(DPCb and NDPCb). Each starting particle set was then used as input for TOPAZ training and extraction[9] and the resulting particles for the DNACb and DPCb datasets were curated using 2D classification (**Figure S20**). The 2D class averages primarily revealed the edges of the cubes, for which there was signal arising from the DNA scaffold and could be readily aligned. Similarly, DPCb exhibited more random coil content as shown by CD spectroscopy (**Figure S13C**, apo DPCb, blue line), indicating disordered peptide organization. Consistent with this, its cryo-EM 2D class averages resulted in projections with poor signal for the polypeptide motif within the cavity of the cube (**Figure S20**). In contrast, NDPCb samples prepared in the presence of $FeSO_4$ and ferroheme demonstrated a more ordered peptide conformation, as indicated by CD analysis (**Figure S13E**, NDPCb, orange line), and resulted in 2D class averages with clear signal inside the cube (**Figure 4G-I)**.

For the NDPCb dataset, particles were curated using Ab Initio Reconstruction and Heterogeneous Refinement, and a final consensus refinement was determined using Non-uniform Refinement (**Figure S21A-C**).[10] 3D Variability Analysis (3DVA) in cluster mode (15Å filter resolution (**Figure S21D**)[11] was then performed to further assess the conformational heterogeneity of the assembly.

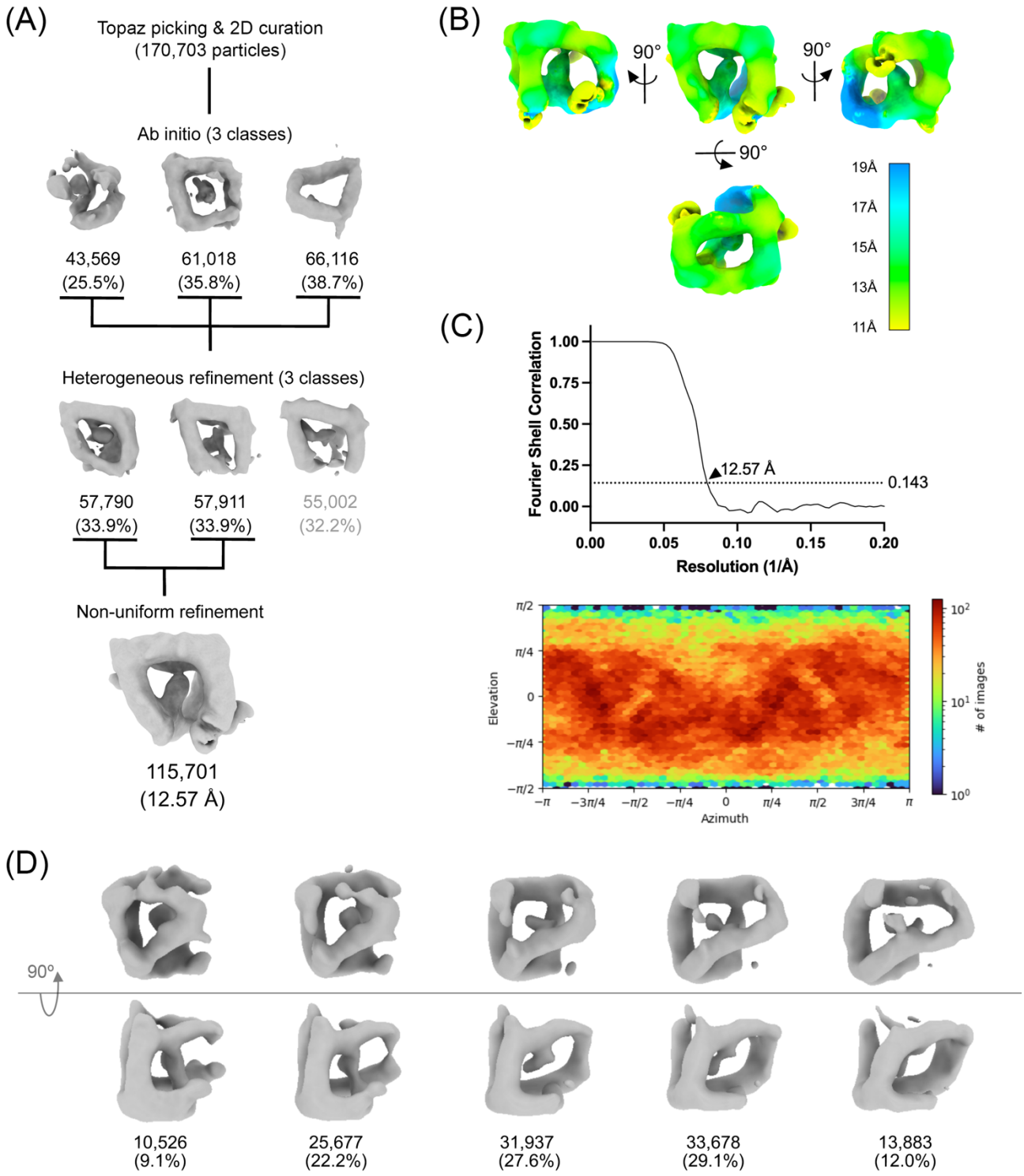

Figure S21. Cryo-EM analysis of the NDPCb sample assembled in the presence of $FeSO_4$ and ferroheme. (A) 3D reconstruction processing pipeline. (B) NDPCb reconstruction colored by local resolution from aquamarine (19 Å) to yellow (11 Å). (C) Fourier Shell Correlation (FSC) plot for the half-maps of the non-uniform refinement. The nominal resolution is determined at FSC = 0.143

(top). Angular distribution heatmap of the particle stack in the final refinement (bottom). (D) Orthogonal views of the classes obtained from the 3D variability analysis.

XIV. DLS results

All constructs were assembled at 1 μM in filtered 1xPBS buffer for DLS analysis. The hydrodynamic size distributions of cubes hybridized to DNA-DBCO (sDNACb) and DNA-Peptide (sDPCb) without 6 T spacers are shown in **Figure S22A**. The DLS plots of cubes containing rigidifying splints and hybridized to DNA-6 T-DBCO (rDNACb) and DNA-6 T-Peptide (rDPCb) are shown in **Figure S22B**. The DLS plots of cube-SNA with varying ratios are presented in **Figure S22C**.

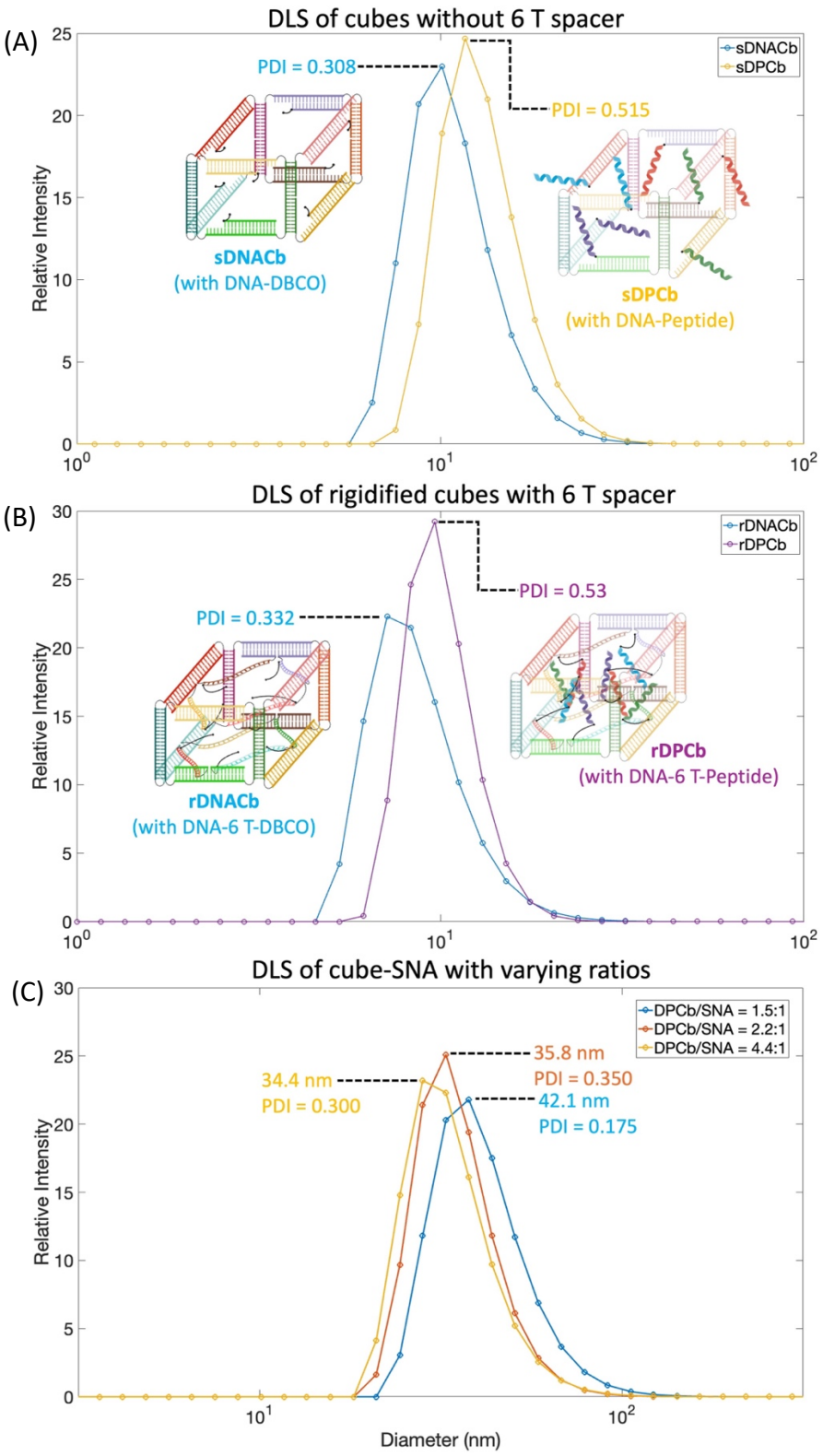

Figure S22. Additional DLS results. (A) DLS plots of sDNACb (blue) and sDPCb (yellow). (B) DLS plots of rDNACb (blue) and rDPCb (purple). (C) DLS plots of cube-SNA complex with varying cube/SNA ratios.

XV. Reference

(1) Poppleton, E.; Romero, R.; Mallya, A.; Rovigatti, L.; Šulc, P. OxDNA.org: a public webserver for coarse-grained simulations of DNA and RNA nanostructures. *Nucleic Acids Res.* **2021**, *49* (W1), W491-W498. DOI: 10.1093/nar/gkab324 (acccessed 7/23/2024).
(2) Asohan, J.; Fakih, H. H.; Das, T.; Sleiman, H. F. Control of the Assembly and Disassembly of Spherical Nucleic Acids Is Critical for Enhanced Gene Silencing. *ACS Nano* **2024**, *18* (5), 3996-4007. DOI: 10.1021/acsnano.3c05940.
(3) Shave, S.; Chen, Y.-K.; Pham, N. T.; Auer, M. PyBindingCurve, Simulation, and Curve Fitting to Complex Binding Systems at Equilibrium. *Journal of Chemical Information and Modeling* **2021**, *61* (6), 2911-2915. DOI: 10.1021/acs.jcim.1c00216.
(4) Kalvet, I.; Ortmayer, M.; Zhao, J.; Crawshaw, R.; Ennist, N. M.; Levy, C.; Roy, A.; Green, A. P.; Baker, D. Design of Heme Enzymes with a Tunable Substrate Binding Pocket Adjacent to an Open Metal Coordination Site. *J. Am. Chem. Soc.* **2023**, *145* (26), 14307-14315. DOI: 10.1021/jacs.3c02742.
(5) Weeratunga, S. K.; Lovell, S.; Yao, H.; Battaile, K. P.; Fischer, C. J.; Gee, C. E.; Rivera, M. Structural Studies of Bacterioferritin B from Pseudomonas aeruginosa Suggest a Gating Mechanism for Iron Uptake via the Ferroxidase Center. *Biochem.* **2010**, *49* (6), 1160-1175. DOI: 10.1021/bi9015204.
(6) Pullin, J.; Wilson, M. T.; Clémancey, M.; Blondin, G.; Bradley, J. M.; Moore, G. R.; Le Brun, N. E.; Lučić, M.; Worrall, J. A. R.; Svistunenko, D. A. Iron Oxidation in Escherichia coli Bacterioferritin Ferroxidase Centre, a Site Designed to React Rapidly with H2O2 but Slowly with O2. *Angew. Chem. Int. Ed.* **2021**, *60* (15), 8361-8369. DOI: https://doi.org/10.1002/anie.202015964.
(7) Schorb, M.; Haberbosch, I.; Hagen, W. J. H.; Schwab, Y.; Mastronarde, D. N. Software tools for automated transmission electron microscopy. *Nature Methods* **2019**, *16* (6), 471-477. DOI: 10.1038/s41592-019-0396-9.
(8) Punjani, A.; Rubinstein, J. L.; Fleet, D. J.; Brubaker, M. A. cryoSPARC: algorithms for rapid unsupervised cryo-EM structure determination. *Nat Methods* **2017**, *14* (3), 290-296. DOI: 10.1038/nmeth.4169.
(9) Bepler, T.; Morin, A.; Rapp, M.; Brasch, J.; Shapiro, L.; Noble, A. J.; Berger, B. Positive-unlabeled convolutional neural networks for particle picking in cryo-electron micrographs. *Nature Methods* **2019**, *16* (11), 1153-1160. DOI: 10.1038/s41592-019-0575-8.
(10) Punjani, A.; Zhang, H.; Fleet, D. J. Non-uniform refinement: adaptive regularization improves single-particle cryo-EM reconstruction. *Nature Methods* **2020**, *17* (12), 1214-1221. DOI: 10.1038/s41592-020-00990-8.
(11) Punjani, A.; Fleet, D. J. 3D variability analysis: Resolving continuous flexibility and discrete heterogeneity from single particle cryo-EM. *Journal of Structural Biology* **2021**, *213* (2), 107702. DOI: https://doi.org/10.1016/j.jsb.2021.107702.